Master Thesis

Computation of gluelump masses for hybrid static potentials in SU(3) Lattice Gauge Theory using the multilevel algorithm

Jannis Herr

Frankfurt am Main, May 2022

Institut für theoretische Physik
Goethe Universität
Frankfurt am Main

Supervisor and first examiner:

Prof. Dr. Marc Wagner

Institut für theoretische Physik

Johann Wolfgang von Goethe Universität Frankfurt am Main

Second examiner:

Prof. Dr. Owe Philipsen

Institut für theoretische Physik

Johann Wolfgang von Goethe Universität Frankfurt am Main

Erklärung nach § 30 (12) Ordnung für den Bachelor- und dem Masterstudiengang

Hiermit erkläre ich, dass ich die Arbeit selbstständig und ohne Benutzung anderer als der angegebenen Quellen und Hilfsmittel verfasst habe. Alle Stellen der Arbeit, die wörtlich oder sinngemäß aus Veröffentlichungen oder aus anderen fremden Texten entnommen wurden, sind von mir als solche kenntlich gemacht worden. Ferner erkläre ich, dass die Arbeit nicht - auch nicht auszugsweise - für eine andere Prüfung verwendet wurde.

Frankfurt, den

Abstract

The aim of this work is to compute gluelump masses for hybrid static potentials in SU(3) Lattice Gauge Theory. For this reason, the form of the gluelump correlation function is discussed in large detail. While states with defined $\mathcal{PC}$ quantum numbers can be constructed, no unique spin identification is possible. Creation operators are constructed such that they transform like irreducible representations of the lattice form of SO(3), the cubic group. Twenty different gluelump masses are computed this way. Computations are performed on four different lattice spacings with $\beta \in \{6.000, 6.284, 6.451, 6.594\}$. Furthermore, the parameters of the multilevel algorithm and APE-smearing are optimized at $\beta = 6.284$. The total number of APE-smearing steps is chosen such that an optimal overlap for higher states is guaranteed. For the multilevel algorithm, several different sublattice structures are compared. Besides that, computations with and without the use of HYP-smearing are performed.

Two different mass extraction procedures, focusing on effective masses and correlation functions respectively, are applied. The masses of the lightest gluelump T_1^{+-} at each lattice spacing are compared with the hybrid static potentials Π_u and Σ_u^-, which were previously computed in [1]. Mass differences are successfully extrapolated to the continuum and possible spin identifications are given. Besides that, two different approaches for the subtraction of the divergent self-energy are applied. One of these approaches focuses on the conversion of the lattice gluelump masses into the RS scheme, which is required for the connection of gluelumps with pNRQCD hybrid potentials.

Contents

1 Introduction

The *strong interaction* is one of the four fundamental forces in nature. The correspondent theory is *Quantum Chromo Dynamics* (QCD), which describes the interaction between quarks and the gauge bosons of QCD, the gluons. The Lagrangian of QCD is derived, by postulating the invariance under certain symmetry transformations, like local SU(3) gauge transformations. The non-abelian character of SU(3) leads to a self-interaction of gluons, which influences the behavior of the coupling constant. At large distances and low energies, it reaches large values, and therefore a perturbative description is not applicable. A possible framework to solve this problem is given by *lattice QCD*, where quarks and gauge fields are discretized on a four-dimensional hypercubic lattice. The computational estimation of observables via Monte-Carlo-based simulations allows the study of further aspects of QCD.

In this work, *gluelump* masses are computed in pure SU(3) Lattice Gauge Theory, where quarks are taken as static color sources. A gluelump is an object consisting of one quark in the adjoint representation and gluons. One of the first gluelump mass computations in SU(2) Lattice Gauge Theory was performed by C. Michael in [2]. Later the spectrum was extended to ten different SU(3) states in [3]. Two former bachelor theses ([4, 5]) focused on gluelump calculation in SU(2) and SU(3) Lattice Gauge Theory respectively. With similar operators like in [6], twenty different gluelump masses are computed in this work. Besides Lattice Gauge Theory, gluelump masses can be determined with different approaches: while [7] explores the spectrum in a simple bag model, [8] and [9] perform computations in the QCD string model and Coulomb gauge QCD respectively.

Even though gluelumps do not exist in full QCD, their masses find application in several different fields. In [3], gluelump masses are identified as *glueballino* masses in the heavy limit, while [10] estimates the string breaking distance of an adjoint potential, using the mass of the lightest gluelump in the SU(2) pseudoparticle approach. Apart from this, [11] identifies gluelump masses as the inverse of the correlation length of the vacuum. Another major application field of gluelumps are *hybrid mesons*.

A hybrid meson is a state, consisting of a quark-antiquark pair and a non-trivial excited gluon field, which contributes to the quantum numbers. This exotic structure can lead to quantum numbers, that differ from the prediction of the constituent quark model. On the lattice, hybrid static potentials approach certain gluelump masses for small $q\bar{q}$-separation distances.

In [1], hybrid static potentials are computed in SU(3) Lattice Gauge Theory. After parametrizing the results, the radial Schrödinger equation is solved with the derived potentials and quark masses, which were taken from quark models, to obtain masses of hybrid mesons.

In [12], a more internally consistent approach is used. Starting from full QCD, a non-relativistic effective field theory for heavy quarkonium hybrids, similar to *potential non-relativistic QCD* (pNRQCD), is constructed. Symmetries are identified in the static limit, while corrections are

obtained in an expansion in terms of the inverse mass of the heavy quark. For the perturbative part of the potential, the RS (*renormalon subtracted*) scheme, is used. It has been worked out for the heavy quark mass in [13] and subtracts the singularities in the Borel plane from the matching coefficients. While working in the RS scheme, all used quantities have to be converted to the RS scheme as well. Gluelump states are required for the construction of the theory and their masses additionally determine the energy scale of hybrid potentials. Therefore, precise mass computations and conversions to the RS scheme are necessary.

Modern literature still uses the RS scheme gluelump masses, which were computed in [13]. The conversion was performed using the lattice results obtained in [3] in the year 1999. The use of the modern clusters *FUCHS-* and *GOETHE-CSC* allows more extensive computations on modern lattice spacings and the application of complex optimization algorithms. Therefore, one aim of this work is to increase the number of computed gluelump masses and enhance the results, especially with the application of the multilevel algorithm [14]. Additionally, this thesis aims to investigate the connection between gluelumps and hybrid static potentials. For this reason, all computations are performed in the same lattice setup, as [1]. Furthermore, mass differences are extrapolated to the continuum, while the mass of the lowest gluelump was estimated via two different approaches.

1.1 Outline

This thesis is organized as follows.
First of all, basic concepts of Lattice Gauge Theory are outlined in Chapter 2. The general introduction is followed by a description of important lattice quantities and the main concepts of Monte Carlo simulations.
Chapter 3 focuses on hybrid static potentials and gluelumps. After an overview of the respective corresponding quantum numbers, continuum gluelump creation operators are discussed. Finally, the lattice gluelump correlation function is presented, while the subsequent discussion focuses on the form of gluelump operators on the lattice.
To achieve more precise results, several different optimization algorithms are applied. HYP-smearing, the multilevel algorithm and APE-smearing are discussed in Chapter 4.
The first half of Chapter 5 focuses on the optimization of the parameters of the multilevel algorithm and APE-smearing. Followed by this, two different mass extraction procedures are applied to the twenty gluelump spectra, computed on each of the four lattice spacings. Finally the mass of the T_1^{+-} gluelump is compared with the hybrid static potentials, computed in [1].
Last but not least, in Chapter 6 mass differences are extrapolated to the continuum. For the derived continuum masses, possible spin identifications are given and the results are compared with [3]. Additionally, the mass of the lightest gluelump is determined via two different approaches. In the end, the results are summarized, followed by an outline.

1.2 Notation

Calculations in this thesis are performed in natural units ($\hbar = c = 1$). Thus, velocities are given in units of the speed of light c and actions in units of $\hbar$. In addition, Einstein's sum convention is used, which implies the summation over duplicate indices.
As common in lattice QCD, the euclidian formulation of QCD is used, where the real time t_{real} is substituted by the complex time $\tau = i \cdot t_{\text{real}}$. This changes the metric to $g_{\mu\nu} = \text{diag}(1, 1, 1, 1)$, which results in the equality of covariant and contravariant vectors/tensors ($A_\mu = A^\mu$). In order to establish a better comparability with the literature, in the following the letters τ, t and x_0 are used for the complex time.

2 Lattice Gauge Theory

This section outlines the general idea behind Lattice Gauge Theory and discusses several important lattice quantities. The discussion is based on reference [15].
The vacuum expectation value of an operator $\mathcal{O}$ in the euclidian formulation of SU(3) gauge theory is given as

$$\langle\Omega|\,\mathcal{O}(A)\,|\Omega\rangle = \frac{1}{Z}\int \mathcal{D}A\ \mathcal{O}(A)\ e^{-S_{\mathrm{G}}(A)} \tag{1}$$

$$Z = \int \mathcal{D}A\ e^{-S_{\mathrm{G}}(A)}, \tag{2}$$

where $|\Omega\rangle$ is the vacuum state, $\int \mathcal{D}A$ denotes the integration over all possible gauge field configurations and $S_G(A)$ is the gluonic part of the QCD-action. Since only static quarks are used, the fermionic part of the action is not needed. S_G can be constructed with the gauge fields $A_\mu = A^a_\mu \lambda^a/2$ by postulating the invariance under local SU(3) gauge transformations. Where λ^a are the Gell-Mann matrices, which are the generators of SU(3) and $a \in \{1, 2, \ldots, 8\}$. The action is defined as

$$S_G = \frac{1}{2g^2}\int \mathrm{d}^4x\, \mathrm{Tr}(F_{\mu\nu}(x)F_{\mu\nu}(x)), \tag{3}$$

with the coupling g and the field strength tensor $F_{\mu\nu}(x)$, which is given as

$$F_{\mu\nu}(x) = -i[D_\mu(x), D_\nu(x)] = \partial_\mu A_\nu(x) - \partial_\nu A_\mu(x) + i[A_\mu(x), A_\nu(x)]. \tag{4}$$

In SU(3) Lattice Gauge Theory, the gauge fields are discretized on a four-dimensional hypercubic lattice Λ

$$\Lambda = \{n = (n_0, n_1, n_2, n_3)|\ n_0 = 0, 1, \ldots, N_T - 1\ ; n_i = 0, 1, \ldots, N - 1\}. \tag{5}$$

The lattice consists of N_T lattice points in temporal direction and N lattice points in each spatial direction, with lattice spacing a. Computations are performed on periodic lattices, which means that $n_i + N = n_i$ and $n_0 + N_t = n_0$. On the lattice, the continuum gauge fields are replaced by link variables $U_\mu \in \mathrm{SU}(3)$, which are visualized in figure 1. They are build from $A_\mu(n)$ via

$$U_\mu(n) \approx \exp(iaA_\mu(n)), \tag{6}$$

with the transformation law

$$U_\mu(n) \to U'_\mu(n) = \Omega(n)U_\mu(n)\Omega(n+\hat{\mu})^\dagger \quad , \quad \Omega \in \mathrm{SU}(3). \tag{7}$$

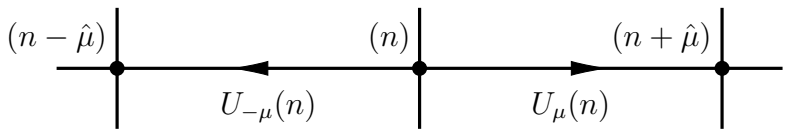

Figure 1: Illustration of the forward link $U_\mu(n)$ and backward link $U_{-\mu}(n)$.

The forward link $U_\mu(n)$ connects the lattice sites (n) and $(n+\hat{\mu})$, while the backward link $U_{-\mu}(n) = U_\mu(n-\hat{\mu})^\dagger$ reaches from (n) to $(n-\hat{\mu})$. For the computation of path integral expectation values on the lattice, one has to express the continuum action (3) in terms of lattice quantities:

$$S_G = \frac{\beta}{3} \sum_{n\in\Lambda} \sum_{\mu<\nu} \mathrm{Re}\,\mathrm{Tr}[\mathbb{1} - U_{\mu\nu}(n)] \quad ; \quad \beta = \frac{6}{g^2} \tag{8}$$

This possible discretization is called *Wilson plaquette action* and it approaches equation (3) for $a \to 0$ with discretization errors of $\mathcal{O}(a^2)$. It is built from a sum of *plaquettes* $U_{\mu\nu}$

$$U_{\mu\nu}(n) = U_\mu(n)\; U_\nu(n+\hat{\mu})\; U_\mu(n+\hat{\nu})^\dagger\; U_\nu(n)^\dagger. \tag{9}$$

2.1 Collection of important lattice quantities

A convenient, but not unique, possible discretization of the field strength tensor is the clover definition [15]

$$F_{\mu\nu}(n) = -\frac{i}{8a^2}(C_{\mu\nu}(n) - C_{\nu\mu}(n)), \tag{10}$$

where $C_{\mu\nu}$ is a so-called cloverleaf sum of plaquettes $U_{\mu\nu}$ in the μ-ν-plane, defined as

$$C_{\mu\nu}(n) = U_{\mu\nu}(n) + U_{\nu-\mu}(n) + U_{-\mu-\nu}(n) + U_{-\nu\mu}(n). \tag{11}$$

The *Wilson loop* $W(r,t)$ is an important quantity for the computation of static potentials. It is built from four pieces, two so-called *Wilson lines* $S(n_t, \mathbf{m}, \mathbf{n})$, $S(0, \mathbf{m}, \mathbf{n})$ and two *temporal transporters* $T(n_t, \mathbf{n})$, $T(n_t, \mathbf{m})$. Each Wilson line connects two spatial lattice points $\mathbf{m}$ and $\mathbf{n}$ along a path $\mathcal{C}_{\mathbf{m},\mathbf{n}}/\mathcal{C}_{\mathbf{n},\mathbf{m}}$ at fixed time n_t and 0, respectively:

$$S(n_t, \mathbf{m}, \mathbf{n}) = \prod_{(\mathbf{k},j)\in\mathcal{C}_{\mathbf{m},\mathbf{n}}} U_j(n_t, \mathbf{k}), \quad \& \quad S(0, \mathbf{n}, \mathbf{m}) = \prod_{(\mathbf{k},j)\in\mathcal{C}_{\mathbf{n},\mathbf{m}}} U_j(0, \mathbf{k}) \tag{12}$$

Each temporal transporter is the product of n_t link variables U_0 in time direction along a straight path at fixed spatial position $\mathbf{n}$ and $\mathbf{m}$, respectively:

$$T(n_t, \mathbf{n}) = \prod_{i=0}^{n_t-1} U_0(i, \mathbf{n}) \quad \& \quad T(n_t, \mathbf{m}) = \prod_{i=0}^{n_t-1} U_0(i, \mathbf{m}) \tag{13}$$

By putting the four parts together and taking the trace, the following equation is obtained:

$$W(|\mathbf{m}-\mathbf{n}|, n_t) = \mathrm{Tr}\left[S(n_t, \mathbf{m}, \mathbf{n}) T(n_t, \mathbf{n})^\dagger S(0, \mathbf{m}, \mathbf{n})^\dagger T(n_t, \mathbf{m})\right]. \tag{14}$$

If the path $\mathcal{C}_{\mathbf{m},\mathbf{n}}$ is a straight line, so if $\mathbf{n}$ and $\mathbf{m}$ lie on the same axis, $W(r,t)$ is called a planar Wilson loop, otherwise non-planar.

2.2 Correlation functions

The correlation function of an operator $\mathcal{O}$, creating a state with certain quantum numbers from the vacuum, is given by

$$C(\tau) = \langle\Omega|\, \mathcal{O}^\dagger(\tau)\mathcal{O}(0)\, |\Omega\rangle\,. \tag{15}$$

This equation can be rewritten by time-evolving the operators and inserting the identity via the completeness of energy eigenstates ($\sum_n |n\rangle\langle n| = 1$):

$$\begin{aligned} C(\tau) &= \sum_n |\underbrace{\langle n|\, \mathcal{O}(0)\, |\Omega\rangle}_{c_n}|^2 \cdot e^{-(E_n - E_\Omega)\cdot\tau} \\ &\overset{\tau\to\infty}{\sim} |c_0|^2 \cdot e^{-(E_0 - E_\Omega)\cdot\tau} \end{aligned} \tag{16}$$

Therefore, the correlation function is an infinite sum of exponential functions of energy differences. For large times one expects the sum to be dominated by the lightest state, i.e. the ground state, with mass $m = E_0 - E_\Omega$. The prefactors $|c_n|^2$ denote the overlap of the state, created by the operator $\mathcal{O}$ from the vacuum, with the n-th state. One possible way to extract masses from correlation functions is by examining the effective mass $m_{\mathrm{eff}}(\tau)$, which reads as

$$a m_{\mathrm{eff}}(\tau) = \ln\left(\frac{C(\tau)}{C(\tau+1)}\right). \tag{17}$$

The expected approach of a plateau for large times can be used to extract the mass of the ground state.

2.3 Monte Carlo simulation and statistical analysis

Even for small lattices and "simple" systems (e.g. Ising spin systems) a direct numerical computation of path integrals is in practice mostly impossible, due to the exponentially increasing number of possible configurations with the lattice volume. For this reason, Monte Carlo simulations are performed, where N gauge field configurations U_n are generated with a heat-bath-algorithm following a probability that is proportional to $\exp(-S[U_n])$. In this thesis, the gauge

field generation started with a so-called *hot start*, where all gauge fields are chosen randomly. After this, the configuration is updated N_{therm} times until it approaches an equilibrium, which means that the configurations follow indeed the desired distribution. Nearby configurations are not completely uncorrelated and therefore do not produce statistically independent results. Because of this, every heath-bath update is followed by N_{or} overrelaxation steps, which is expected to minimize correlations between subsequent configurations. Additionally, every measurement is separated by N_{sep} updates. Further details about the general ideas of the above-described algorithms and their implementation are given in [15].
The path integral is then evaluated by averaging over all generated configurations.

$$\langle \mathcal{O} \rangle = \frac{1}{Z} \int \mathcal{D}[U] e^{-S_G[U]} \mathcal{O}[U] \approx \frac{1}{N} \sum_{U_n} \mathcal{O}[U_n] \tag{18}$$

If the configurations are independent, the errors are proportional to $(1/\sqrt{N})$. Thus, quadrupling N will double the precision. The statistical error of effective masses and correlation functions, in the following general denoted as y, is estimated, using the *jackknife method*:

A sample of measurements consists of N elements y_i, where $y_i \in \{y_1, y_2, \ldots, y_N\}$. The average $\bar{y}$ of the full measurement is then given as

$$\bar{y} = \frac{1}{N} \sum_{i=1}^{N} y_i. \tag{19}$$

One can construct N new values y_i', by deleting the i-th element of the whole dataset and calculating the average:

$$y_i' = \frac{1}{N-1} \sum_{\substack{j=1 \\ j \neq i}}^{N} y_j \tag{20}$$

The error estimate of the observable is then given as

$$\sigma_y = \sqrt{\frac{N-1}{N} \sum_{i=1}^{N} (\bar{y} - y_i')^2}. \tag{21}$$

The previously described methods provide the necessary basis for the computation of physical observables, such as hybrid static potentials and gluelump masses.

3 Hybrid static potentials and gluelumps

This short introduction about quantum numbers of hybrid static potentials and gluelumps is mainly based on [1], [13] and [16].
The ordinary static potential, which describes the potential between an infinitely heavy quark-antiquark pair separated by a distance r, can be computed on the lattice via Wilson loops $W(r,t)$ (cf. eq. (14)). In the case of hybrid static potentials, the string connecting the $q\bar{q}$ pair is excited. Therefore, one has to replace the spatial transporters in a planar Wilson loop $W(r,t)$ with more complex link paths. Thus, it is possible to take the additional contributions to its quantum numbers into account. These quantum numbers are typically classified as follows:

- $\Lambda = \Sigma(=0), \Pi(=1), \Delta(=2), \Phi(=3), \ldots$ is the total angular momentum with respect to the quark-antiquark axis.
- $\eta = g(=+), u(=-)$ is defined as the behavior under the combination of parity and charge conjugation $\mathcal{P} \circ \mathcal{C}$.
- $\epsilon = +, -$ denotes the eigenvalue of a reflection $\mathcal{P}_x$ along a coordinate axis perpendicular to the $q\bar{q}$ pair separation axis.

In this notation, the ordinary static potential is classified as Σ_g^+. Because states with $\Lambda \geq 1$ are degenerated with respect to ϵ, the subscript is usually omitted for $\Lambda \neq \Sigma$. The belonging symmetry group is the group of cylindrical rotations with reflection $D_{\infty h}$.
A point-like QCD state is characterized by the $J^{\mathcal{PC}}$ [1] of the rotation group $O(3)\otimes\mathcal{C}$ and the gauge group representation of the source. States created by operators in the singlet representation are called glueballs, while octet states are called gluelumps.
Because $D_{\infty h} \subset O(3) \otimes \mathcal{C}$, in the limit $r \to 0$ certain hybrid levels must become degenerated [13]. The expected degeneracies of hybrid potentials at short distances are shown in table 1. In section 5.4.3 the behavior of Σ_u^- and Π_u is shown, which belong to a $J^{\mathcal{PC}} = 1^{+-}$ state with $J_z = 0$ and $J_z \pm 1$, respectively. In this limit, source and anti-source will be at the same lattice site and their color can be combined in a gauge-invariant way ($\mathbf{3} \otimes \mathbf{3}^* = \mathbf{8} \oplus \mathbf{1}$) creating an octet (gluelump correlator) and a singlet (glueball correlator) [17]. Thus, for a Wilson loop corresponding to the correlator of a hybrid static potential in the small separation limit, the following manner is expected:

$$\lim_{r\to 0} W_{\text{hybrid}}(r,t) = c_1 \cdot e^{-m_{\text{gl}}\cdot t} + c_2 \cdot e^{-m_{\text{gb}}\cdot t} \tag{22}$$

Here, m_{gl} and m_{gb} correspond to the mass of a gluelump/glueball. The correlator given in equation (22) is dominated by the lighter state for large t. In most cases of present interest,

[1] J denotes the angular momentum of the point-like state.

gluelumps with given $J^{\mathcal{PC}}$ are lighter than glueball states. Hence, the gluelump state is expected to dominate the given correlator for large times. Therefore, it is necessary to measure the gluelump spectrum to predict the behavior of hybrid static potentials for small r's. In section 6.2.2, the connection between gluelump masses and hybrid potentials in the RS scheme is shown.

Point particle $J^{\mathcal{PC}}$	Hybrid potential Λ_η^ϵ
1^{+-}	Σ_u^-,Π_u
1^{--}	$\Sigma_g^{+\prime}$,Π_g
2^{--}	Σ_g^-,Π_g',Δ_g
2^{+-}	Σ_u^+,Π_u',Δ_u
3^{+-}	$\Sigma_u^{-\prime}$,Π_u'',Δ_u', Φ_u
0^{++}	$\Sigma_g^{+\prime\prime}$

Table 1: Expected degeneracies of hybrid potentials at short distance, based on the level ordering of the gluelump spectrum. Taken from [13].

3.1 Gluelumps in the continuum

It is not possible to build a gauge-invariant operator consisting of one quark/color source in the fundamental representation and gluons. The transformation behavior of a color source reads as

$$\begin{pmatrix} Q_1 \\ Q_2 \\ Q_3 \end{pmatrix} \to g(\alpha) \begin{pmatrix} Q_1 \\ Q_2 \\ Q_3 \end{pmatrix}, \quad g(\alpha) = \exp\left(i\alpha_a \frac{\lambda^a}{2}\right) \in \mathrm{SU}(3). \tag{23}$$

A possible way of avoiding this problem is to choose a color source in the adjoint representation. For this case, the color source is mapped into the adjoint representation ($Q_a = Q_a^3 \to Q_a^{(8)}$) resulting in not just having $N = 3$, but $N^2 - 1 = 8$ degrees of freedom. Therefore, the adjoint representation of SU(2) is three-dimensional, SU(3) has eight dimensions, and so on.
Equation (23) then has the following form

$$\begin{pmatrix} Q_1^{(8)} \\ Q_2^{(8)} \\ \vdots \\ Q_8^{(8)} \end{pmatrix} \to g(\alpha) \begin{pmatrix} Q_1^{(8)} \\ Q_2^{(8)} \\ \vdots \\ Q_8^{(8)} \end{pmatrix}, \quad g(\alpha) = \exp(i\alpha_a T^a), \tag{24}$$

where the top index is explicitly written down to clarify, that the fields are in the octet representation. The 8×8 matrices T^a are generating the adjoint representation. The adjoint quark and the given transformation law under gauge transformations read as

$$Q_{\mathrm{adj}} = Q_a^{(8)} \frac{\lambda_a}{2} \to g(\alpha) Q_{\mathrm{adj}} g(\alpha)^\dagger. \tag{25}$$

In order to show that equation (24) and (25) can be transformed into each other, one has to use the quantity

$$\mathrm{Tr}(Q_{\mathrm{adj}}\lambda^a) = \mathrm{Tr}\left(Q_a \frac{\lambda^a}{2}\lambda^b\right) = \frac{Q_a}{2}\underbrace{\mathrm{Tr}(\lambda^a\lambda^b)}_{2\delta_{ab}} = Q_b, \tag{26}$$

where the condition that the Gell-Mann matrices λ^a are orthogonal under the trace of their product was applied and the index [(8)] was omitted for better readability. As common in group theory, equation (24) is expressed for infinitesimal transformations (i.e. $\alpha_i \ll 1$), while inserting the transformation law of equation 25.

$$\begin{aligned}
Q_d = \mathrm{Tr}(Q_{\mathrm{adj}}\lambda^d) &\to \mathrm{Tr}\left(\exp\left(i\alpha_a\frac{\lambda^a}{2}\right) Q_b \frac{\lambda^b}{2} \exp\left(-i\alpha_c\frac{\lambda^c}{2}\right)\lambda^d\right) \\
&\approx \mathrm{Tr}\left(\left(\mathbb{1} + i\alpha_a\frac{\lambda^a}{2}\right) Q_b \frac{\lambda^b}{2}\left(\mathbb{1} - i\alpha_c\frac{\lambda^c}{2}\right)\lambda^d\right) \\
&\approx \mathrm{Tr}\left(\frac{Q_b}{2}\left(\lambda^b + i\frac{\alpha_a}{2}\lambda^a\lambda^b - i\frac{\alpha_c}{2}\lambda^b\lambda^c\right)\lambda^d\right) \\
&= Q_d + \mathrm{Tr}\left(\frac{Q_b}{2} i\frac{\alpha_a}{2}\underbrace{[\lambda^a,\lambda^b]}_{2if^{abc}\lambda^c}\lambda^d\right) \\
&= Q_d - \frac{Q_b}{2}\alpha_a f^{abc}\,\mathrm{Tr}(\lambda^c\lambda^d) = Q_d - Q_b\alpha_a f^{abd}
\end{aligned} \tag{27}$$

Here, $\approx$ always indicates that terms of $\mathcal{O}(\alpha_i^2)$ were neglected, and f^{abc} are the antisymmetric structure constants of SU(3). According to [18], the structure constants of a fundamental representation are related to the generators of the adjoint representation via

$$f^{abc} = i(T_a)_{bc}. \tag{28}$$

With this expression and the antisymmetric behavior of the structure constants, equation 27 finally becomes

$$Q_d \to Q_d + i\alpha_a(T_a)_{db}Q_b. \tag{29}$$

But this is just the infinitesimal form of equation 24. Thus both expressions are equivalent. After this proof, possible gluelump operators can be written down. A possible choice is

$$\mathcal{O}(x) = \mathrm{Tr}(Q_{\mathrm{adj}}(x)B_x(x)). \tag{30}$$

In principle, the chromo-magnetic field could be replaced with other combinations of covariant derivatives and components of the field strength tensor. Examples with given spin and quantum numbers are shown in table 2.

The required gauge-invariance of operators can be shown, using the transformation law of a magnetic field under gauge transformations

$$B_x(x) = F^a_{23}\frac{\lambda^a}{2} \to g(x)B_x(x)g(x)^\dagger, \quad g(x) \in \mathrm{SU}(3). \tag{31}$$

Now it is easy to see that $\mathcal{O}(x)$ is indeed gauge-invariant

$$\mathcal{O}(x) \to \mathrm{Tr}(g(x)Q_{\mathrm{adj}}(x)g(x)^\dagger g(x)B_x(x)g(x)^\dagger) = \mathcal{O}(x), \tag{32}$$

where the property that $g(x)$ are SU(3) matrices (e.g. $g(x)g(x)^\dagger = \mathbb{1}$) and the invariance of the trace under cyclic permutations were used.

$J^{\mathcal{PC}}$	Creation operator
1^{+-}	B_i
1^{--}	E_i
2^{--}	$D_{\{i}B_{j\}}$
2^{+-}	$D_{\{i}E_{j\}}$
3^{+-}	$D_{\{i}D_jB_{k\}}$
0^{++}	$\mathbf{B}^2$

Table 2: Possible creation operators for a gluelump state with quantum numbers $J^{\mathcal{PC}}$. The curly braces denote complete symmetrization of the indices which means that all symmetric permutations are summed up. Taken from [13].

3.2 Gluelumps on the lattice

In the following section, the behavior of the gluelump correlation function on the lattice is investigated. It can be obtained by replacing continuum quantities with lattice expressions and integrating over the adjoint static $q\bar{q}$ pair. The gluelump correlation function is, according to reference [6], given by

$$C(\tau_2 - \tau_1) = H^\alpha(\tau_1) L^{\alpha\beta}(\tau_1, \tau_2) H^{\beta\dagger}(\tau_2). \tag{33}$$

All constituents of equation (33) are defined at the same spatial lattice site $\mathbf{n}$. They have the definitions

$$H^\alpha(\tau) = \mathrm{Tr}(G(\tau) T^\alpha) \quad ; \quad H^{\beta\dagger}(\tau) = \mathrm{Tr}(G(\tau)^\dagger T^\beta) \tag{34}$$

and

$$L^{\alpha\beta}(\tau_1, \tau_2) = U_0^{(8)\alpha\gamma}(\tau_1) U_0^{(8)\gamma\epsilon}(\tau_1 + a) \dots U_0^{(8)\rho\beta}(\tau_2 - a). \tag{35}$$

Here, $G(\tau) = G(\tau, \mathbf{n})$ is a suiting linear combination of spatial closed loops of links that create/destroy states with certain quantum numbers. They are discussed in section 3.5. $T^a = \lambda^a/2$ are the generators of SU(3), while $L^{\alpha\beta}(\tau_1, \tau_2)$ is defined as a product of adjoint temporal links connecting τ_1 and τ_2. $U_0^{(8)\alpha\gamma}$ are temporal links mapped into the adjoint representation via

$$U_0^{(8)\alpha\beta} = \mathrm{Tr}(T^\alpha U_0 T^\beta U_0^\dagger). \tag{36}$$

To achieve a better comparability with older gluelump works (e.g. [19]), $Q(\tau_1, \tau_2)$ is defined as the product of fundamental temporal links connecting the lattice sites $(\tau_1, \mathbf{n})$ and $(\tau_2, \mathbf{n})$. Equation (35) can be simplified by using the following relation [20] for the generators of SU(N)

$$T^\alpha_{ij} T^\alpha_{kl} = \delta_{il}\delta_{jk} - \frac{1}{N}\delta_{ij}\delta_{kl}. \tag{37}$$

The product of two adjoint links in the time direction is given as

$$L^{\alpha\beta}(\tau_1, \tau_1 + 2a) = U_0^{(8)\alpha\gamma}(\tau_1) U_0^{(8)\gamma\beta}(\tau_1 + a). \tag{38}$$

Using equations 36 and 37 with $N = 3$, this leads to

$$\begin{aligned} L^{\alpha\beta}(\tau_1, \tau_1 + 2a) &= \mathrm{Tr}(T^\alpha U(\tau_1) T^\gamma U^\dagger(\tau_1)) \,\mathrm{Tr}(T^\gamma U(\tau_1 + a) T^\beta U^\dagger(\tau_1 + a)) \\ &= T^\alpha_{ab} U(\tau_1)_{bc} T^\gamma_{cd} U^\dagger(\tau_1)_{da} \cdot T^\gamma_{ef} U(\tau_1 + a)_{fg} T^\beta_{gh} U^\dagger(\tau_1 + a)_{he} \\ &= U(\tau_1)_{bc} U(\tau_1 + a)_{fg} U^\dagger(\tau_1)_{da} U^\dagger(\tau_1 + a)_{he} T^\alpha_{ab} T^\beta_{gh} \left(\delta_{cf}\delta_{de} - \frac{1}{3}\delta_{cd}\delta_{ef}\right). \end{aligned} \tag{39}$$

Here the short form $U = U_0$ was used.

Evaluating the first term of equation (39) results in

$$\begin{aligned} & U(\tau_1)_{bc}U(\tau_1+a)_{fg}U^\dagger(\tau_1)_{da}U^\dagger(\tau_1+a)_{he}T^\alpha_{ab}T^\beta_{gh}\ \delta_{cf}\delta_{de} \\ &= U(\tau_1)_{bc}U(\tau_1+a)_{cg}U^\dagger(\tau_1)_{da}U^\dagger(\tau_1+a)_{hd}T^\alpha_{ab}T^\beta_{gh} \\ &= [U(\tau_1)U(\tau_1+a)]_{bg}T^\beta_{gh}[U(\tau_1)U(\tau_1+a)]^\dagger_{ha}T^\alpha_{ab} \\ &= \mathrm{Tr}(Q(\tau_1,\tau_1+2a)T^\beta Q^\dagger(\tau_1,\tau_1+2a)T^\alpha). \end{aligned} \tag{40}$$

The second term can be rearranged as

$$\begin{aligned} & -\frac{1}{3}U(\tau_1)_{bc}U(\tau_1+a)_{fg}U^\dagger(\tau_1)_{da}U^\dagger(\tau_1+a)_{he}T^\alpha_{ab}T^\beta_{gh}\ \delta_{cd}\delta_{ef} \\ &= -\frac{1}{3}\underbrace{U(\tau_1)_{bc}U^\dagger(\tau_1)_{ca}}_{=\delta_{ab}}\underbrace{U^\dagger(\tau_1+a)_{he}U(\tau_1+a)_{eg}}_{=\delta_{gh}}T^\alpha_{ab}T^\beta_{gh} \\ &= -\frac{1}{3}T^\alpha_{aa}T^\beta_{gg}=0, \end{aligned} \tag{41}$$

where the condition that the generators of SU(N) are traceless, was used. This leads to the following conclusion

$$L^{\alpha\beta}(\tau_1,\tau_2)=\left(\prod_{\tau=\tau_1}^{\tau_2-a}U_0^{(8)}(\tau)\right)^{\alpha\beta}=Q^{(8)\alpha\beta}(\tau_1,\tau_2). \tag{42}$$

In words, this means that the product of adjoint links in the time direction is the same as multiplying fundamental temporal links and then mapping them into the adjoint representation. With this expression equation (33) simplifies to

$$C(\tau_2-\tau_1)=\mathrm{Tr}(G(\tau_1)T^\alpha)\,\mathrm{Tr}(T^\alpha Q T^\beta Q^\dagger)\,\mathrm{Tr}(G(\tau_2)^\dagger T^\beta). \tag{43}$$

Last but not least, a new form of the correlation function, which is more convenient for computation, is derived:

$$
\begin{aligned}
C(\tau_2-\tau_1) &= \mathrm{Tr}(G(\tau_1)T^\alpha)\,\mathrm{Tr}(T^\alpha Q T^\beta Q^\dagger)\,\mathrm{Tr}(G(\tau_2)^\dagger T^\beta) \\
&= G(\tau_1)_{ab}T^\alpha_{ba}T^\alpha_{cd}Q_{de}T^\beta_{ef}Q^\dagger_{fc}G(\tau_2)^\dagger_{gh}T^\beta_{hg} \\
&= G(\tau_1)_{ab}Q_{de}Q^\dagger_{fc}G(\tau_2)^\dagger_{gh}\cdot\left(\delta_{bd}\delta_{ac}-\frac{1}{3}\delta_{ab}\delta_{cd}\right)\cdot\left(\delta_{eg}\delta_{hf}-\frac{1}{3}\delta_{ef}\delta_{gh}\right) \\
&= G(\tau_1)_{ad}Q_{dg}G(\tau_2)^\dagger_{gf}Q^\dagger_{fa}-\frac{1}{3}G(\tau_1)_{aa}\underbrace{Q_{dg}Q^\dagger_{fd}}_{=\delta_{fg}}G(\tau_2)^\dagger_{gf} \\
&\quad -\frac{1}{3}G(\tau_1)_{ad}\underbrace{Q_{df}Q^\dagger_{fa}}_{=\delta_{da}}G(\tau_2)^\dagger_{hh}+\frac{1}{9}G(\tau_1)_{aa}\underbrace{Q_{df}Q^\dagger_{fd}}_{=\delta_{dd}=3}G(\tau_2)^\dagger_{hh} \\
&= \mathrm{Tr}[G(\tau_1)QG(\tau_2)^\dagger Q^\dagger]-\frac{1}{3}\,\mathrm{Tr}[G(\tau_1)]\,\mathrm{Tr}[G(\tau_2)^\dagger] \\
&\quad -\frac{1}{3}\,\mathrm{Tr}[G(\tau_1)]\,\mathrm{Tr}[G(\tau_2)^\dagger]+\frac{1}{3}\,\mathrm{Tr}[G(\tau_1)]\,\mathrm{Tr}[G(\tau_2)^\dagger] \\
&= \mathrm{Tr}[G(\tau_1)QG(\tau_2)^\dagger Q^\dagger]-\frac{1}{3}\,\mathrm{Tr}[G(\tau_1)]\,\mathrm{Tr}[G(\tau_2)^\dagger]
\end{aligned}
\tag{44}
$$

For better understanding, equal terms are marked with the same color. With the gauge transformation law of the above quantities

$$
\begin{aligned}
G(\tau,\mathbf{n}) &\to G'(\tau,\mathbf{n}) = \Omega(\tau,\mathbf{n})G(\tau,\mathbf{n})\Omega(\tau,\mathbf{n})^\dagger \\
Q(\tau_1,\tau_2,\mathbf{n}) &\to Q'(\tau_1,\tau_2,\mathbf{n}) = \Omega(\tau_1,\mathbf{n})Q(\tau_1,\tau_2,\mathbf{n})\Omega(\tau_2,\mathbf{n})^\dagger,
\end{aligned}
\tag{45}
$$

one can see that $C(\tau_2-\tau_1)$ is indeed gauge-invariant.

3.3 Building $\mathcal{PC}$-eigenstates

The linear combination $G(\tau)$, mentioned in equation (44), consists of several closed link paths. To classify them the same notation given in [21] is used.
Let C_i be a path of length L, corresponding to a space like Wilson loop operator $\mathcal{O}_i$. For the following discussion, only the shape and orientation of the path are of importance. C_i can be represented by a L-tuple

$$(\hat{f}_1, \ldots, \hat{f}_L) \quad \text{with} \quad \sum_{i=1}^{L} \hat{f}_i = 0, \tag{46}$$

where the vectors $\hat{f}_i$ are given as $\hat{f}_i \in \{\pm\hat{e}_j \mid j = 1, 2, 3\}$. $\hat{e}_i$ correspond to the unit vectors of spacelike coordinates on the lattice. In this notation the path given in figure 2 is noted as $(\hat{e}_x, \hat{e}_y, \hat{e}_z, -\hat{e}_x, -\hat{e}_z, -\hat{e}_y)$.

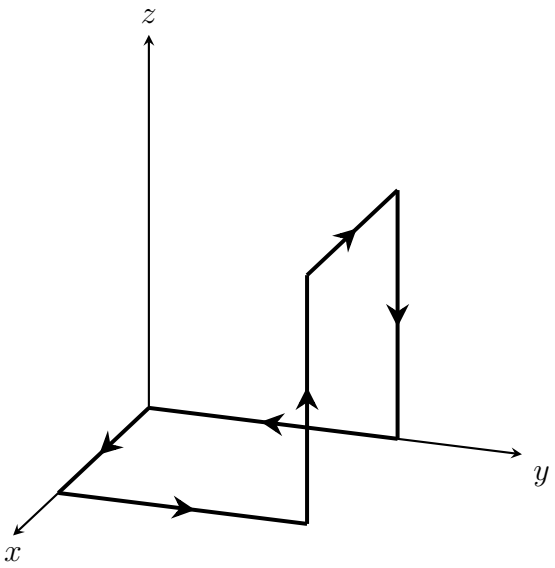

Figure 2: Example of a closed loop, classified as $(\hat{e}_x, \hat{e}_y, \hat{e}_z, -\hat{e}_x, -\hat{e}_z, -\hat{e}_y)$.

In the continuum, the gauge fields A_μ transform as follows under charge conjugation transformations $\mathcal{C}$

$$A_\mu \xrightarrow{\mathcal{C}} -A_\mu^T. \tag{47}$$

Thus, the following manner of the tuple under charge conjugation on the lattice is expected:

$$\mathcal{C}(\hat{f}_1, \ldots, \hat{f}_L) = (-\hat{f}_L, -\hat{f}_{L-1} \ldots, -\hat{f}_1) \tag{48}$$

The influence of this transformation is also illustrated in figure 3. One can now easily construct $\mathcal{C}$-eigenstates

$$(\hat{f}_1, \ldots, \hat{f}_L)_{\mathcal{C}=\pm} = (\hat{f}_1, \ldots, \hat{f}_L) \pm (-\hat{f}_L, \ldots, -\hat{f}_1). \tag{49}$$

Numerically this can be done with little effort. One has to compute the path C_i and add or subtract the hermetian transpose of itself, for positive or negative $\mathcal{C}$-parity, respectively.
For $\mathcal{P}$-eigenstates one can carry out the same procedure. The transformation law reads as

$$\mathcal{P}(\hat{f}_1, \ldots, \hat{f}_L) = (-\hat{f}_1, \ldots, -\hat{f}_L). \tag{50}$$

This is no surprise, since the parity transformation corresponds to a spatial reflection (cf. figure 3). Analogously, parity eigenstates are constructed

$$(\hat{f}_1, \ldots, \hat{f}_L)^{\mathcal{P}=\pm} = (\hat{f}_1, \ldots, \hat{f}_L) \pm (-\hat{f}_1, \ldots, -\hat{f}_L). \tag{51}$$

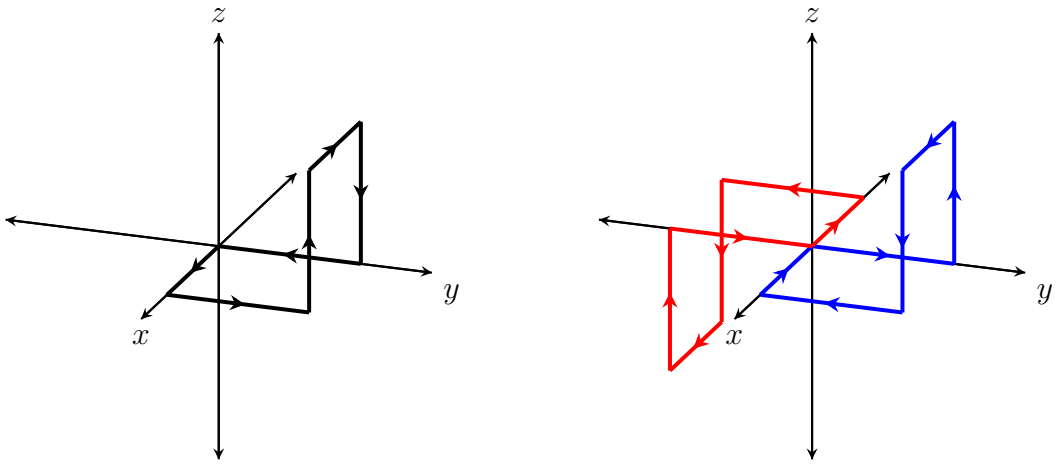

Figure 3: Illustration of the different symmetry operations on the original black path $(\hat{e}_x, \hat{e}_y, \hat{e}_z, -\hat{e}_x, -\hat{e}_z, -\hat{e}_y)$. The parity transformed path $(-\hat{e}_x, -\hat{e}_y, -\hat{e}_z, \hat{e}_x, \hat{e}_z, \hat{e}_y)$ is marked in red, while the charge conjugated path $(\hat{e}_y, \hat{e}_z, \hat{e}_x, -\hat{e}_z, -\hat{e}_y, -\hat{e}_x)$ is colorized in blue.

Combining equations (48) and (51), the rule for constructing $\mathcal{PC}$-eigenstates for a path C_i can be stated:

$$(\hat{f}_1, \ldots, \hat{f}_L)^{\mathcal{P}=\pm}_{\mathcal{C}=\pm} = \Big[(\hat{f}_1, \ldots, \hat{f}_L) \pm (-\hat{f}_1, \ldots, -\hat{f}_L)\Big] \pm \Big[(-\hat{f}_L, \ldots, -\hat{f}_1) \pm (\hat{f}_L, \ldots, \hat{f}_1)\Big] \tag{52}$$

Please note, that all given states have to be normalized.

3.4 The cubic group

This section is based on [21], [22] and [23].

Due to the lattice discretization, the symmetry group of a gluelump is no longer SO(3) with $\mathcal{C}$-partiy, because it is not possible to rotate around arbitrary angles, but discrete values. The associated symmetry group is called O and contains 24 elements. The direct product of the O with parity (which is of order two) is called O_h.

Each of the non-identity elements of the cubic group O can be interpreted as a rotation around a uniquely determined symmetry axis of a cube [21]. The only point of symmetry in a cube is the center, which is fixed under the application of all elements and is complemented by 13 symmetry axes $C_n^{(i)}$. In general, the order n of an axis is defined as the number of rotations, which can be performed around this axis (including the identity), while the index (i) labels the different possible axes. They are illustrated in figure 4. Note that every axis is passing through the point of symmetry.

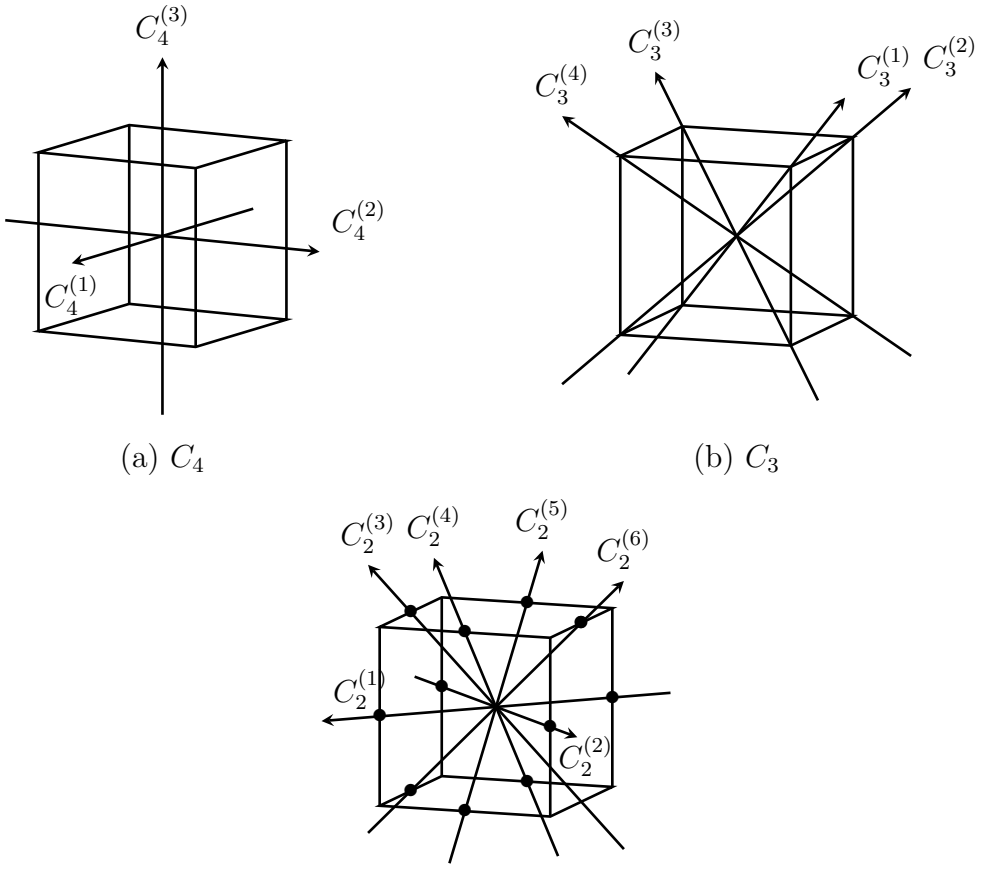

(a) C_4 (b) C_3

(c) C_2

Figure 4: Illustration of all 13 symmetry axes of a cube. Dots are drawn for C_2-rotations to mark the position where the axes cross the edges.

There are three axes perpendicular to the faces of the cube and one can perform four rotations by $\frac{\pi}{2}$ along these axes. Thus, they are called $C_4^{(i)}$, $i = (1, 2, 3)$. Furthermore, there are four axes connecting two vertices of the cube. Three rotations by $\frac{2\pi}{3}$ are possible, hence they are called $C_3^{(i)}$, $i = (1, 2, 3, 4)$. Last but not least, one can construct six axes connecting two centers of edges, where two rotations by an angle π are realizable with the name $C_2^{(i)}$, $i = (1, \ldots, 6)$.
With this knowledge, the number of independent elements N, which is the sum of all possible distinguishable rotations, plus the identity, can be determined. This leads to

$$N = \underbrace{1}_{\text{id}} + \underbrace{3 \cdot (4-1)}_{C_4^{(i)}} + \underbrace{4 \cdot (3-1)}_{C_3^{(i)}} + \underbrace{6 \cdot (2-1)}_{C_2^{(i)}} = 24. \tag{53}$$

The five classes of conjugate elements mC_n of the cubic group are given as:

- $E = \{\text{id}\}$: Identity
- $6C_2 = \{C_2^{(i)}(\varphi)\}$ with $i \in \{1, \ldots, 6\}$ and $\varphi = \pi$
- $8C_3 = \{C_3^{(i)}(\varphi), (C_3^{(i)}(\varphi))^2\}$ with $i \in \{1, 2, 3, 4\}$ and $\varphi = \pm\frac{2\pi}{3}$
- $6C_4 = \{C_4^{(i)}(\varphi), (C_4^{(i)}(\varphi))^3\}$ with $i \in \{1, 2, 3\}$ and $\varphi = \pm\frac{\pi}{2}$
- $3C_4^2 = \{(C_4^{(i)}(\varphi))^2\}$ with $i \in \{1, 2, 3\}$ and $\varphi = \pi$

Here m denotes the total number of elements and n is the same quantity as given above. Note that two elements $a, b \in G$ of a group G are conjugate if $b = g^{-1}ag$ for a $g \in G$. The conjugacy class of an element a is then defined as $\text{Cl}(a) = \{g^{-1}ag \mid g \in G\}$.
These five conjugacy classes correspond to the existence of five irreducible representations with dimension d_j respectively. According to the theorem of Burnside the squared dimension must add up to the order of the group, i.e.

$$\sum_{j=1}^{5} d_j^2 = 24. \tag{54}$$

The only solution for the representation dimensions is $d_j = (1, 1, 2, 3, 3)$, with names A_1, A_2, E, T_1 and T_2 respectively. In this notation A_1 is the trivial representation while T_1 is the standard vector representation. The correspondent characters[2] χ are shown in table 3.

[2]The character $\chi^{\mathcal{R}}(g)$ of $g \in G$ in a given representation $\mathcal{R}$ is defined as: $\chi^{\mathcal{R}}(g) = \text{Tr}\,\mathcal{R}(g)$

Λ	$\chi(E)$	$\chi(6C_2)$	$\chi(8C_3)$	$\chi(6C_4)$	$\chi(3C_4^2)$
A_1	1	1	1	1	1
A_2	1	-1	1	-1	1
E	2	0	-1	0	2
T_1	3	-1	0	1	-1
T_2	3	1	0	-1	-1
$\theta(\xi)$	2π	π	$2\pi/3$	$\pi/2$	π

Table 3: Characters $\chi(\xi)$ for all irreducible representations Λ with a given rotation angle $\theta(\xi)$ [24].

On the lattice it is not possible to associate an operator, transforming like an irreducible representation $\Lambda \in \{A_1, A_2, E, T_1, T_2\}$, to a unique spin. Each representation can, but must not, contain several spins. In table 4 the possible corresponding spins for each irreducible representation Λ are shown. The following formula allows the subduction of continuum J to discrete Λ of O [24]

$$n_\Lambda^J = \frac{1}{N} \sum_\xi m_\xi \chi^{(\Lambda)}(\xi)^* \chi^{(J)}(\xi). \tag{55}$$

Here, N is the order of the group, m_ξ the number of elements for a given ξ and $\chi^{(J)}(\xi)$ the character for spin J and rotation angle $\theta(\xi)$ to class ξ given by

$$\chi^{(J)}(\xi) = \frac{\sin\left[\left(J + \frac{1}{2}\right)\theta(\xi)\right]}{\sin\left(\frac{\theta(\xi)}{2}\right)}. \tag{56}$$

Table 4 is then derived using equation (55) and table 3.

Representation	Dimension	Angular momentum
A_1	1	$J = 0, 4, 6, 8, \ldots$
A_2	1	$J = 3, 6, 7, 9, \ldots$
E	2	$J = 2, 4, 5, 6, \ldots$
T_1	3	$J = 1, 3, 4, 5, \ldots$
T_2	3	$J = 2, 3, 4, 5, \ldots$

Table 4: Irreducible representations with corresponding angular momenta and dimensions.

3.5 Gluelump creation operators on the lattice

With this knowledge, possible gluelump operators can be built. For this purpose, one has to start with a spatial closed Wilson loop and list all 24 possible octahedral rotations of it. One possible way is to choose the standard plaquette as a starting object like it was done in [3]. Operators are then built as linear combinations of quadratic loops, which share one corner, such that they transform as irreducible representations Λ. $\mathcal{PC}$-eigenstates $\Lambda^{\mathcal{PC}}$ are then created using the methods described in section 3.3. One can also use the coefficients given in table 5 for construction, by ignoring the third direction. A benefit of these types of operators is that they can be implemented numerically with low effort. For instance, the linear combination for building the T_1^{+-} gluelump in the y,z-plane is given as

$$G(T_{1x}^{+-}) = U_{23} - U_{32} + U_{3-2} - U_{-23} + U_{-2-3} - U_{-3-2} + U_{-32} - U_{2-3}. \tag{57}$$

Note that every object is defined at the lattice site $(\tau, \mathbf{n})$. This is just the same linear combination of plaquettes as in the clover discretization of the field strength tensor (eq. (10)). The downside of this type of operator is that only 10 out of 20 possible $\Lambda^{\mathcal{PC}}$ can be constructed. This is due to the fact, that some $\mathcal{PC}$-transformations are equivalent to octahedral rotations. Table 6 shows which irreducible representations are possible for a given shape.

To solve this problem the operators of [6], which are 1×2-rectangles bent in the middle (cf. fig. 2), are adapted. Due to their lower symmetry, all 20 $\Lambda^{\mathcal{PC}}$ possibilities can be built. In figure 5 all used paths for the construction of the gluelump creation operators are shown, while the path coefficients are given in table 5. For a better readability a shorter notation was used:

$$(\hat{e}_i, \hat{e}_j, \hat{e}_k, -\hat{e}_i, -\hat{e}_k, -\hat{e}_j) \to (i, j, k) \tag{58}$$

A (six tuple) chair-shaped path is described every time the three tuple form is used. To build a state with positive parity one has to form the combination $(A + B)$, while negative $\mathcal{P}$ states are built from $(A - B)$. One has to add or subtract the hermitian transpose for positive or negative charge parity states. The linear combinations for each irreducible representation are given as follows [6]:

$$
\begin{aligned}
G(A_1) &= \sum_{a=1}^{24} L_a^{(8)}\,, \\
G(A_2) &= \sum_{a=1}^{12} (-1)^a L_a^{(8)} - \sum_{a=13}^{24} (-1)^a L_a^{(8)}\,, \\
G(T_{1x}) &= L_6^{(8)} + L_{20}^{(8)} + L_{21}^{(8)} + L_{11}^{(8)} - L_{18}^{(8)} - L_8^{(8)} - L_9^{(8)} - L_{23}^{(8)}\,, \\
G(T_{1y}) &= L_5^{(8)} + L_{19}^{(8)} + L_{24}^{(8)} + L_{10}^{(8)} - L_{17}^{(8)} - L_7^{(8)} - L_{12}^{(8)} - L_{22}^{(8)}\,, \\
G(T_{1z}) &= L_1^{(8)} + L_2^{(8)} + L_3^{(8)} + L_4^{(8)} - L_{13}^{(8)} - L_{14}^{(8)} - L_{15}^{(8)} - L_{16}^{(8)}\,, \\
G(T_{2x}) &= L_6^{(8)} - L_{20}^{(8)} + L_{21}^{(8)} - L_{11}^{(8)} + L_{18}^{(8)} - L_8^{(8)} + L_9^{(8)} - L_{23}^{(8)}\,, \\
G(T_{2y}) &= L_5^{(8)} - L_{19}^{(8)} + L_{24}^{(8)} - L_{10}^{(8)} + L_{17}^{(8)} - L_7^{(8)} + L_{12}^{(8)} - L_{22}^{(8)}\,, \\
G(T_{2z}) &= L_1^{(8)} - L_2^{(8)} + L_3^{(8)} - L_4^{(8)} + L_{13}^{(8)} - L_{14}^{(8)} + L_{15}^{(8)} - L_{16}^{(8)}\,, \\
G(E_1) &= v^x - v^y\,, \\
G(E_2) &= v^x + v^y - 2v^z\,, \\
v^x &= L_6^{(8)} + L_{20}^{(8)} + L_{21}^{(8)} + L_{11}^{(8)} + L_{18}^{(8)} + L_8^{(8)} + L_9^{(8)} + L_{23}^{(8)}\,, \\
v^y &= L_5^{(8)} + L_{19}^{(8)} + L_{24}^{(8)} + L_{10}^{(8)} + L_{17}^{(8)} + L_7^{(8)} + L_{12}^{(8)} + L_{22}^{(8)}\,, \\
v^z &= L_1^{(8)} + L_2^{(8)} + L_3^{(8)} + L_4^{(8)} + L_{13}^{(8)} + L_{14}^{(8)} + L_{15}^{(8)} + L_{16}^{(8)}\,.
\end{aligned} \tag{59}
$$

For a given correlation function of a representation Λ with dimension d_Λ, one has to average over all dimensions and lattice sites, to obtain a projection to zero momentum

$$
C(\tau,\Lambda) = \frac{1}{Z} \sum_{d=1}^{d_\Lambda} \sum_{t=0}^{N_T-1} \sum_{n_1,n_2,n_3=0}^{N-1} C(\tau,\mathbf{n},\Lambda_d) \quad ; \quad Z = d_\Lambda \cdot N^3 \cdot N_T. \tag{60}
$$

The derivation of the orthonormal bases is based on group theoretical methods and is technical and long, but straightforward (cf. [21]). Therefore, we decided, that it is more clear, to derive the character relations for a given irreducible representation, in order to see if the built states are indeed transforming like irreducible representations Λ. Besides that, the above-given sums, agree with others in literature specified creation operators (e.g. [25].)

A_1 and A_2 are one-dimensional, thus, the correspondent rotation matrices are one-dimensional as well. As mentioned above, A_1 is a scalar state. Hence it should behave like a scalar under rotations. This rotational invariance was achieved by summing up all possible rotations and results in all characters being one.
A_2 is built from a slightly different sum. All chairs corresponding to C_2 and C_4 rotations are subtracted, while all C_3 and C_4^2 rotations are added. Thus, for example a C_2 rotation will change the sign of the sum. Again the characters agree with table 3.

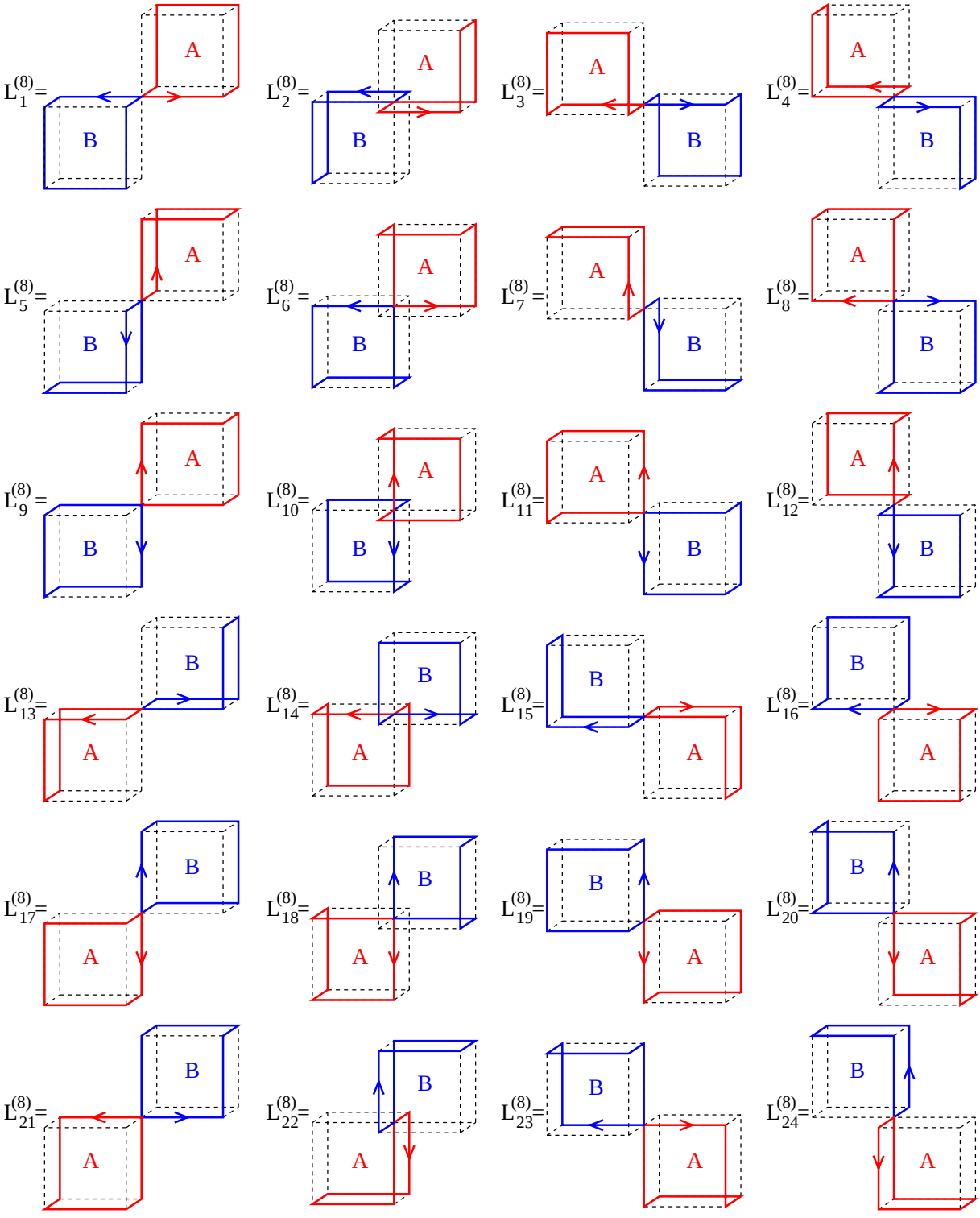

Figure 5: All chair-shaped paths for creating gluelump operators. Dotted lines are drawn to guide the eye. Path B is the parity reflection of path A. The index $^{(8)}$ indicates that these paths correspond to octet states. Taken from [6].

Since T_1 and T_2 are three-dimensional, the rotation matrices are three-dimensional as well. The character is defined as the trace of the rotation matrices in a given representation. Thus, to determine the characters, one only has to compute the diagonal elements. Note that T_{1i} and T_{2i} are built from the same eight chairs, but again differ in signs. Examples for the following mentioned rotations are shown in figure 6. Since T_{1i} states are invariant under rotations around the i-axis, an illustration as planes is possible, where sum elements with sign $\pm$ are denoted as $T_{1i}^{(\pm)}$.

It is clear to see that a C_4 rotation around the z-axis has not any impact on T_{1z}. Hence, the $(3,3)$-element of the transformation matrix must be one. Rotating T_{1x} and T_{1y} will not return the element itself, but $\pm T_{1y}$ and $\pm T_{1x}$, respectively (depending on the chosen rotation direction). Thus, the diagonal-elements (1,1) and (2,2) are zero. This results in the character being one, as shown in the character table.

T_{1i} consists of one upper part with a positive sign and one lower part with a negative sign. A C_4^2 rotation around the i-axis will then have no impact on the element i but will change the sign of the other two T_1-objects. The diagonal-elements are then -1,-1 and 1 and $\chi(C_4^2) = -1$.

Obtaining $\chi(E)$ is trivial since it is always equal to the dimension of a representation. For C_2 rotation axes tangent to cube faces parallel to the i-axis, the sign changes in the T_{1i} representation. The other two representations are converted into $\pm$ of each other. Thus, the only diagonal element is minus one, which results in $\chi(C_2) = -1$.

In contrast to this, C_3 rotations will transform T_{1i} into T_{1j} with $j \neq i$, corresponding to $\chi(C_2) = 0$. This concludes the proof that the above given operators are indeed transforming like the irreducible representation T_1.

The characters of T_2 only differ for two rotation classes. Unlike T_1, chairs in the same plane differ alternately in signs. Thus, a rotation around the i-axis will change the sign in the T_{2i} representation, which leads to $\chi(C_4) = -1$.

The effect of a C_2-rotation is for T_{2i} very similar to T_{1i}, with the difference that the alternating signs in the same plane result in the only diagonal element being one ($\rightarrow \chi(C_2) = 1$). The derivation of the characters of E is shown in [6]. Another possibility for computing the characters is by implementing the cubic rotations numerically with quaternions like it was done in reference [26].

Numerical computations have shown, that a proper mass determination was only possible for operators with a larger extension. Table 6 shows for what kind of operator a mass extraction could be performed. An extension of 2 denotes that the chosen path is for instance $(\hat{e}_x, \hat{e}_x, \hat{e}_y, \hat{e}_y, \hat{e}_z, \hat{e}_z, -\hat{e}_x, -\hat{e}_x \ldots, -\hat{e}_y)$. For even higher extension no significant improvement in the noise/signal ratio was found, which led to the use of operators with an extension of 2 in the following computations.

Chair number	Path	Chair number	Path
1	$(y, -x, z)$	13	$(x, -y, -z)$
2	(x, y, z)	14	$(-y, -x, -z)$
3	$(-y, x, z)$	15	$(-x, y, -z)$
4	$(-x, -y, z)$	16	$(y, x, -z)$
5	$(-x, z, y)$	17	$(-z, x, -y)$
6	(y, z, x)	18	$(-z, -y, -x)$
7	$(x, z, -y)$	19	$(-z, -x, y)$
8	$(-y, z, -x)$	20	$(-z, y, x)$
9	$(z, y, -x)$	21	$(-y, -z, x)$
10	(z, x, y)	22	$(-x, -z, -y)$
11	$(z, -y, x)$	23	$(y, -z, x)$
12	$(z, -x, -y)$	24	$(x, -z, y)$

Table 5: Coefficients for the chair-shaped paths shown in figure 5.

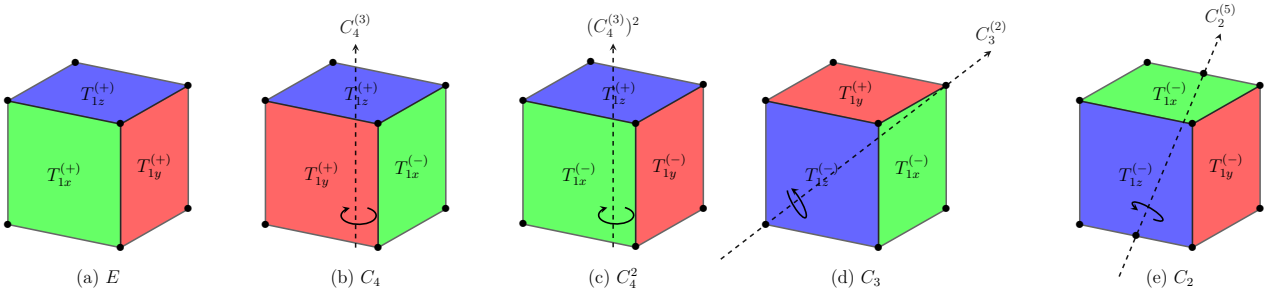

(a) E (b) C_4 (c) C_4^2 (d) C_3 (e) C_2

Figure 6: One example rotation for all types of possible rotations of a T_1 state. Since T_1 components are invariant under rotations in the same plane, they can be illustrated as colorized planes. In addition the rotation axis with rotation direction, that led to the shown cube orientation, is shown.

Operator	Pl.	Chair, size 1	Chair, size 2	Operator	Pl.	Chair, size 1	Chair, size 2
A_1^{++}	✓	✓	✓	E^{-+}	x	✓	✓
A_1^{+-}	x	x	✓	E^{--}	x	✓	✓
A_1^{-+}	x	x	✓	T_1^{++}	x	x	✓
A_1^{--}	x	x	✓	T_1^{+-}	✓	✓	✓
A_2^{++}	x	x	✓	T_1^{-+}	✓	✓	✓
A_2^{+-}	✓	✓	✓	T_1^{--}	✓	✓	✓
A_2^{-+}	x	✓	✓	T_2^{++}	✓	x	✓
A_2^{--}	x	x	✓	T_2^{+-}	x	✓	✓
E^{++}	✓	✓	✓	T_2^{-+}	✓	✓	✓
E^{+-}	✓	x	✓	T_2^{--}	✓	✓	✓

Table 6: Information if a proper mass extraction from an operator built with a given shape was possible. "Pl." denotes a plaquette-shaped path, while "Chair, size i", is a chair-shaped path with extension i.

3.6 Gluelumps in SU(N)

The calculations performed in section 3.2 can be extended to SU(N). By simplifying

$$C(\tau_2 - \tau_1) = \mathrm{Tr}(G(\tau_1)T^\alpha)\,\mathrm{Tr}(T^\alpha Q T^\beta Q^\dagger)\,\mathrm{Tr}(G(\tau_2)^\dagger T^\beta), \tag{61}$$

one can obtain

$$C(\tau_2 - \tau_1) = \mathrm{Tr}[G(\tau_1)QG(\tau_2)^\dagger Q^\dagger] - \frac{1}{N}\,\mathrm{Tr}[G(\tau_1)]\,\mathrm{Tr}[G(\tau_2)^\dagger]. \tag{62}$$

One major difference between SU(2) and SU(3) can be explored by inserting explicitly the generators for $N = 2$ into equation (61):

$$C(\tau_2 - \tau_1) \propto \mathrm{Tr}(G(\tau_1)\sigma^\alpha)\,\mathrm{Tr}(\sigma^\alpha Q \sigma^\beta Q^\dagger)\,\mathrm{Tr}(G(\tau_2)^\dagger \sigma^\beta) \tag{63}$$

But $G(\tau)$ are SU(2) matrices, which means that they can be expressed in terms of the Pauli matrices σ^α with real prefactors h_α

$$G(\tau) = h_0 \cdot \mathbb{1} + i \sum_j h_j \sigma^j, \tag{64}$$

where $h_0^2 + \sum_j h_j^2 = 1$. With this relation one can analyze $\mathrm{Tr}(G(\tau)\sigma^a)$, which leads to

$$\mathrm{Tr}(G(\tau)\sigma^a) = h_0 \cdot \underbrace{\mathrm{Tr}(\sigma^a)}_{=0} + i \sum_j h_j \underbrace{\mathrm{Tr}(\sigma^j \sigma^a)}_{2\delta_{ja}} = 2ih_a = -\,\mathrm{Tr}(G(\tau)^\dagger \sigma^a). \tag{65}$$

Hence $\mathrm{Tr}[(G(\tau) + G(\tau)^\dagger)\sigma^a] = 0$, which is just the linear combination with $\mathcal{C} = +$. Hence, in SU(2) Lattice Gauge Theory only negative charge parity gluelumps exist.

4 Numerical improvement

In this section, several improvement techniques for the lattice results are discussed. These methods aim to increase the overlap with the ground state (APE-smearing), reduce the divergent self-energy (HYP-smearing) and decrease the noise in the temporal transporters (multilevel algorithm).

4.1 APE-smearing

APE-smearing [27] is a common technique in lattice QCD to increase the overlap of the "lattice state" with the ground state to extract proper ground state masses at small times. The procedure was developed by the APE collaboration and can be repeated repetitively. For the following discussion, the notation given in [28] is used. In step N_s the link variable $U_\mu^{(N_s-1)}(x)$ is replaced by

$$U_\mu^{(N_s)}(x) = P_{\mathrm{SU(3)}}\left[(1-\alpha_s)U_\mu^{(N_s-1)}(x) + \frac{\alpha_s}{6}S_\mu^{(N_s-1)}(x)\right], \tag{66}$$

where $P_{\mathrm{SU(3)}}$ denotes the projection to SU(3). α_s is a weighting factor that is commonly chosen as $\alpha_s = 0.5$ and $S_\mu^{(N_s-1)}$ is a so-called staple, that reads as

$$S_\mu^{(N_s-1)}(x) = \sum_{\pm\nu\neq\mu} U_\nu^{(N_s-1)}(x)U_\mu^{(N_s-1)}(x+\hat{\nu})U_\nu^{(N_s-1)}(x+\hat{\mu})^\dagger. \tag{67}$$

One can see that the above quantity is the sum of all shortest paths connecting the lattice sites (x) and $(x+\hat{\mu})$ without the use of the direct link. All spatial links used in this thesis are smeared using the APE procedure, with parameters optimized in section 5.2.
With optimized N_s one would expect the following manner for a state created by a gluelump operator $\mathcal{O}\,|\Omega\rangle$:

$$|\langle 1|\,\mathcal{O}\,|\Omega\rangle\,|^2, |\langle 2|\,\mathcal{O}\,|\Omega\rangle\,|^2, \ldots, |\langle n|\,\mathcal{O}\,|\Omega\rangle\,|^2 \ll |\langle 0|\,\mathcal{O}\,|\Omega\rangle\,|^2 \tag{68}$$

4.2 HYP-smearing

A gluelump is localized in the temporal direction down to the lattice spacing. This leads to an unphysical self-energy, which is expected to be, similar to the self-energy of a quark-antiquark pair, proportional to $\frac{1}{\beta a}$ [29]. This additional contribution to the mass results in faster-decreasing correlation functions, which correspond to a smaller signal/noise ratio for large t.

The HYP-smearing (*hypercubic blocking*) procedure [30] improves this behavior by reducing the self-energy. For this reason, the final so-called *hypercubic fat links* $V_\mu(x)$ are constructed via projected APE blocking from a set of decorated links $\tilde{V}_{\mu;\nu}(x)$

$$V_\mu(x) = P_{\mathrm{SU(3)}}\left[(1-\alpha_1)U_\mu(x) + \frac{\alpha_1}{6}\sum_{\pm\nu\neq\mu}\tilde{V}_{\nu;\mu}(x)\tilde{V}_{\mu;\nu}(x+\hat{\nu})\tilde{V}^\dagger_{\nu;\mu}(x+\hat{\mu})\right], \tag{69}$$

where the indices μ and ν in $\tilde{V}_{\mu;\nu}(x)$ indicate that the decorated link has direction μ and only contains staples that do not extend in ν-direction. They can be constructed analogously by another set of different decorated links $\bar{V}_{\rho;\nu\,\mu}(x)$

$$\tilde{V}_{\mu;\nu}(x) = P_{\mathrm{SU(3)}}\left[(1-\alpha_2)U_\mu(x) + \frac{\alpha_2}{4}\sum_{\pm\rho\neq\nu,\mu}\bar{V}_{\rho;\nu\,\mu}(x)\bar{V}_{\mu;\rho\,\nu}(x+\hat{\rho})\bar{V}^\dagger_{\rho;\nu\,\mu}(x+\hat{\mu})\right]. \tag{70}$$

Here the same notation as above is used, which means that the decorated link $\bar{V}_{\rho;\nu\,\mu}(x)$ is pointing in the ρ-direction and does not contain staples in ν- or μ-direction. They are constructed from the non-smeared links $U_\mu(x)$ via

$$\bar{V}_{\mu;\nu\,\rho}(x) = P_{\mathrm{SU(3)}}\left[(1-\alpha_3)U_\mu(x) + \frac{\alpha_3}{2}\sum_{\pm\eta\neq\rho,\nu,\mu}U_\eta(x)U_\mu(x+\hat{\eta})U^\dagger_\eta(x+\hat{\mu})\right]. \tag{71}$$

In figure 7, a three-dimensional schematic representation of the three previously described steps is presented.

The input parameters α_i can be varied for optimal results. In the computations, HYP-smeared temporal links with $\vec{\alpha} = (1.0, 1.0, 0.5)$ were used.

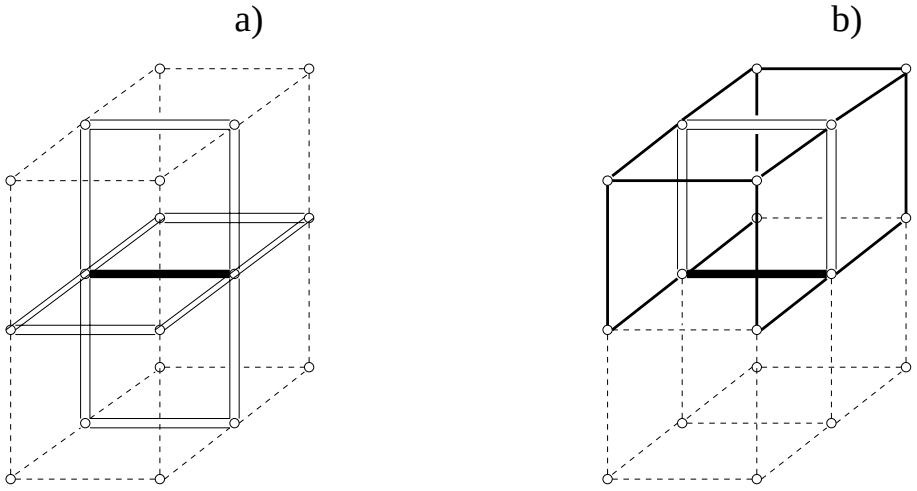

Figure 7: The continuously drawn paths on the right hand side are used to construct one double-lined staple. Four of this kind are then used for building the fat link (cf. a)). Taken from [30].

4.3 The multilevel algorithm

The multilevel algorithm was originally developed by Lüscher and Weisz in [14] and exploits the locality of SU(3) to exponentially decrease statistical errors for the computation of Wilson or Polyakov loops.

4.3.1 Two-link operators

An important quantity in the context of the multilevel algorithm is the *two-link operator*, which is defined at the lattice site $x = (x_0, 0, 0, 0)$ as follows

$$\mathbf{T}(x_0)_{\alpha\beta\gamma\delta} = U_0(x)^*_{\alpha\beta} U_0(x + r\hat{1})_{\gamma\delta}. \tag{72}$$

Please note that the following discussion is performed for a Wilson loop in the x_0-x_1-plane with corners $(0,0), (t,0), (t,r), (0,r)$, but an extension for general Wilson loops is not difficult. The multiplication of a pair of two-link operators can be performed via

$$\{\mathbf{T}(x_0)\mathbf{T}(x_0 + a)\}_{\alpha\beta\gamma\delta} = \mathbf{T}(x_0)_{\alpha\lambda\gamma\epsilon}\mathbf{T}(x_0 + a)_{\lambda\beta\epsilon\delta}. \tag{73}$$

Using this rule one can rewrite a Wilson loop as

$$W(r,t) = S(0)_{\alpha\gamma} \{\mathbf{T}(0)\mathbf{T}(a)\dots\mathbf{T}(t-a)\}_{\alpha\beta\gamma\delta} S(t)^*_{\beta\delta}, \tag{74}$$

with the line operator $S(x_0)_{\alpha\beta} = \{U_1(x)\dots U_1(x + (r-a)\hat{1})\}_{\alpha\beta}$.

4.3.2 Sublattice expectation values

A time-slice consists of all lattice points with time coordinates in the interval $[x_0, y_0]$. For a sublattice expectation value, the spatial links at the boundaries are held fixed, while the link variables in the interior are the degrees of freedom. A sublattice expectation value on a given time-slice is then marked with square brackets [...] and is given by

$$[\mathbf{T}(x_0)\dots\mathbf{T}(y_0-a)] = \frac{1}{Z_{\text{sub}}}\int D[U]_{\text{sub}}\mathbf{T}(x_0)\dots\mathbf{T}(y_0-a)e^{-S[U]_{\text{sub}}}. \tag{75}$$

This can be taken even further with more levels, by expressing two-link operator averages as sublattice expectation values of smaller partitioned sublattices. Such averages are then compatible in the sense, that they satisfy

$$[\mathbf{T}(x_0)\mathbf{T}(x_0+a)] = [[\mathbf{T}(x_0)]\,[\mathbf{T}(x_0+a)]]\,. \tag{76}$$

The correlation function of a gluelump is different compared to a Wilson loop. One can try to rewrite the first term of equation (44) in terms of two-link operators.

$$\begin{aligned} C_{\text{first}}(T) &= \text{Tr}\left(G(0)QG(T)^\dagger Q^\dagger\right) \\ &= G(0)_{ij}Q^*_{il}Q_{jk}G(T)^\dagger_{kl} \end{aligned} \tag{77}$$

But $Q^*_{il}Q_{jk}$ is just a two-link operator with extension zero. This leads to

$$C_{\text{first}}(T) = G(0)_{ij}\mathbf{T}(x_0, r=0)_{iljk}G(T)^\dagger_{kl}. \tag{78}$$

4.3.3 The algorithm

The computations were performed with the codebase developed by Christian Reisinger, which was used in [31] and adapted to our purposes. Thus, the same notation is used.
For the multilevel algorithm, a lattice with temporal extension N_T is partitioned into n_{ts} time-slices with thicknesses $p_1, p_2, \dots p_{n_{\text{ts}}}$, with $\sum_j p_j = N_T$. In the case of more levels each of the n_{ts} time-slices with thickness p_j is partitioned into smaller slices of thickness $p_{j;i}$, where $\sum_i p_{j;i} = p_j$. Figure 8 shows a possible partitioning for a two-level scheme. Please note that brackets, that denote sublattice averages, are colorized in the same color as the sublattice itself.
For every top-level gauge field configuration n_m sublattice configurations are generated by updating the links in the interior $n_m \cdot n_u$ times. This means, that all sublattice configurations are separated by n_u updates. Performing this procedure for higher-order schemes would require that for every sublattice configuration $n_{m,2}$ subsublattice configurations are generated, which are separated by $n_{u,2}$ updates. This process has to be repeated until the lowest level is reached. On the lowest level, one has to compute the time-slice averages of two-link operators. The

expectation values are then used to calculate averages on a higher level (cf. eq. (76)). One has to repeat these steps until the top level is reached.
With these averages a calculation of correlation function values with equation (44) and (78) is possible. The algorithm is repeated for every top-level configuration.

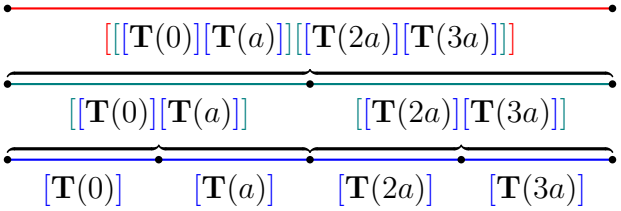

Figure 8: Illustration of the averaging of two-link operators in a two level scheme. For better visibility spatial links are not displayed.

4.3.4 Exponential error reduction

In the following Lüscher's reasoning, why an exponential error reduction appears for the expectation value $[\mathbf{T}(x_0)\mathbf{T}(x_0+a)]$, while the time-slices are in the confinement phase, is outlined.
The expected value of a Polyakov line can be specified using the multilevel algorithm (with time-slice thickness $2a$ and extension N_T) as follows

$$\left\langle P^*(x)P(x+r\hat{1})\right\rangle = \left\langle [\mathbf{T}(0)\mathbf{T}(a)]\dots[\mathbf{T}(N_T-2a)\mathbf{T}(N_T-a)]\right\rangle . \tag{79}$$

If the time-slices are in the confinement phase, the following applies

$$\|[\mathbf{T}(x_0)\dots\mathbf{T}(y_0-a)]\| \propto e^{-m_0 r}, \tag{80}$$

where $\|\dots\|$ denotes a norm for 9×9-matrices acting on complex vectors. Now, if n_m measurements are made on each sublattice, the error is proportional to $1/n_m^{1/2}$. One can choose n_m such that the signal/error ratio is equal to one:

$$n_m \propto e^{2m_0 r} \tag{81}$$

The errors of the single factors in equation (79) would then be proportional to $e^{-m_0 r}$, which corresponds to the error of a Polyakov line with length N_T to equal

$$\sigma \propto e^{-m_0 r N_T/2a}. \tag{82}$$

Thus, the errors are exponentially reduced with the area $A = r\cdot N_T$.
Even though the algorithm turned out to improve gluelump mass results (cf. sec. 5.3), a few issues with this discussion in general and in the context of gluelumps, exist.

According to [15] the expectation value of Polyakov loops $\langle P \rangle$ at large separation distances can be used to determine whether a system is in the confinement phase:

- $\langle P \rangle = 0 \longleftrightarrow$ confinement
- $\langle P \rangle \neq 0 \longleftrightarrow$ no confinement

In figure 9 the Polyakov loop expectation value as a function of the temperature T (defined in eq. (83)) in MeV, which can be varied by changing the extension p_j of the sublattice, is shown.

$$T = \frac{1}{p_j \cdot a} \tag{83}$$

Hence, for temperatures lower than $T_c \approx 270$MeV the system is in the confinement phase and the argumentation of Lüscher is applicable. In this context one has to choose for instance $p_j = 12$ at $\beta = 6.284$ to reach temperatures lower than T_c. But this is, in our experience, way too thick for proper spectroscopy and p_j has to be even larger for smaller lattice spacings.
On the one hand equation, equation (80) is not completely the same as a Polyakov loop expectation value, since it is not forming a closed loop around a periodic lattice. On the other hand, gluelumps define Wilson loops for $r \to 0$. Thus an exponential reduction with the area $A = r \cdot N_T$ might have no influence.
Therefore, clarifying why the multilevel algorithm works in the case of gluelumps requires further investigation.

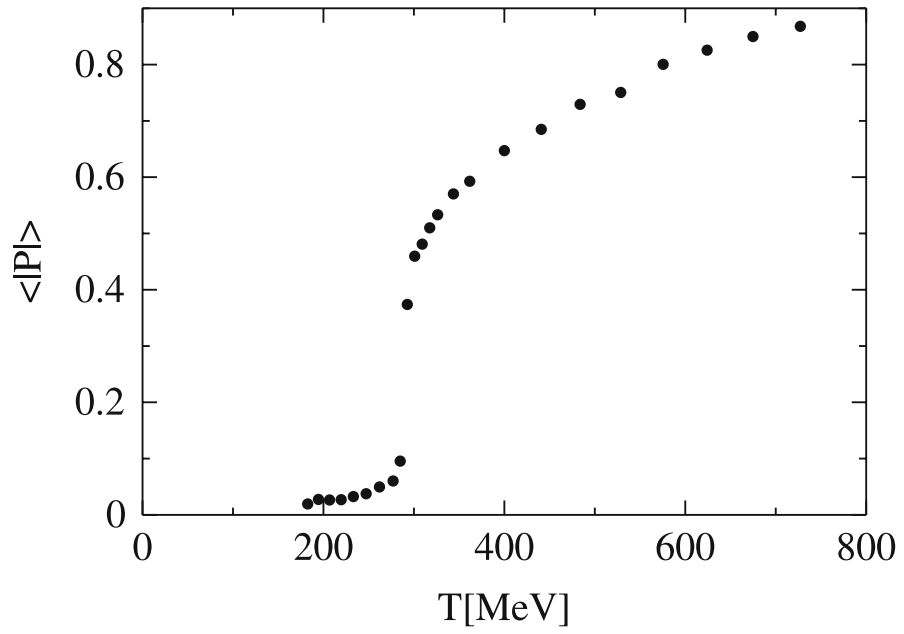

Figure 9: Polyakov loop expectation value as a function of the temperature T in MeV. Taken from [15].

5 Lattice results

5.1 Lattice setup

The aim of this work is not only to compare gluelump masses with hybrid static potentials but also to extrapolate the data into the continuum. For this reason, a cross-check, if the lattice spacings used in [1] are small enough to neglect errors of $\mathcal{O}(a^4)$, is performed.
Because every gluelump mass contains the same amount of divergent self-energy, differences of gluelump masses have a finite value for $a \to 0$. Usually masses are given relative to the lightest gluelump T_1^{+-}.
Therefore, the following ansatz for the mass splitting data of T_1^{--} and T_1^{+-}, taken from [3], is chosen

$$\Delta m = m_0 + c_2 \cdot a^2 + c_4 \cdot a^4. \tag{84}$$

Figure 10 shows the results of the fit. It is clear to see, that the used lattice spacing a_1 is way too large for approximating the continuum with only a quadratic term. The impact of $\mathcal{O}(a^4)$ is significant for $a \approx a_1$. All lattice spacings used in this thesis are smaller than/equal to a_2. Thus we are confident, that our lattice spacings are sufficiently small enough for a proper quadratic continuum extrapolation.
Table 7 shows the four ensembles A, B, C and D used in this thesis, which were generated with the CL2QCD software package [32] in reference [1]. The lattice spacing a was related to the Sommer scale r_0 via the following parametrization, derived in [33]

$$\begin{aligned} \ln(a/r_0) = &- 1.6804 - 1.7331(\beta - 6) + 0.7849(\beta - 6)^2 - 0.4428(\beta - 6)^3, \\ &\text{for } 5.7 \leq \beta \leq 6.92. \end{aligned} \tag{85}$$

As common in pure gauge theory, r_0 was set to 0.5fm. The number of lattice points was chosen for each ensemble, such that the lattice volume is $\approx (1.2\text{fm})^3 \cdot 2.4\text{fm}$, which turned out to be large enough to neglect finite volume corrections. In addition, the ensembles were negatively tested for possible topological freezing. Thus, we are sure that the used gauge field configurations are of high quality. Two sets of computations with HYP-smearing and without were performed.

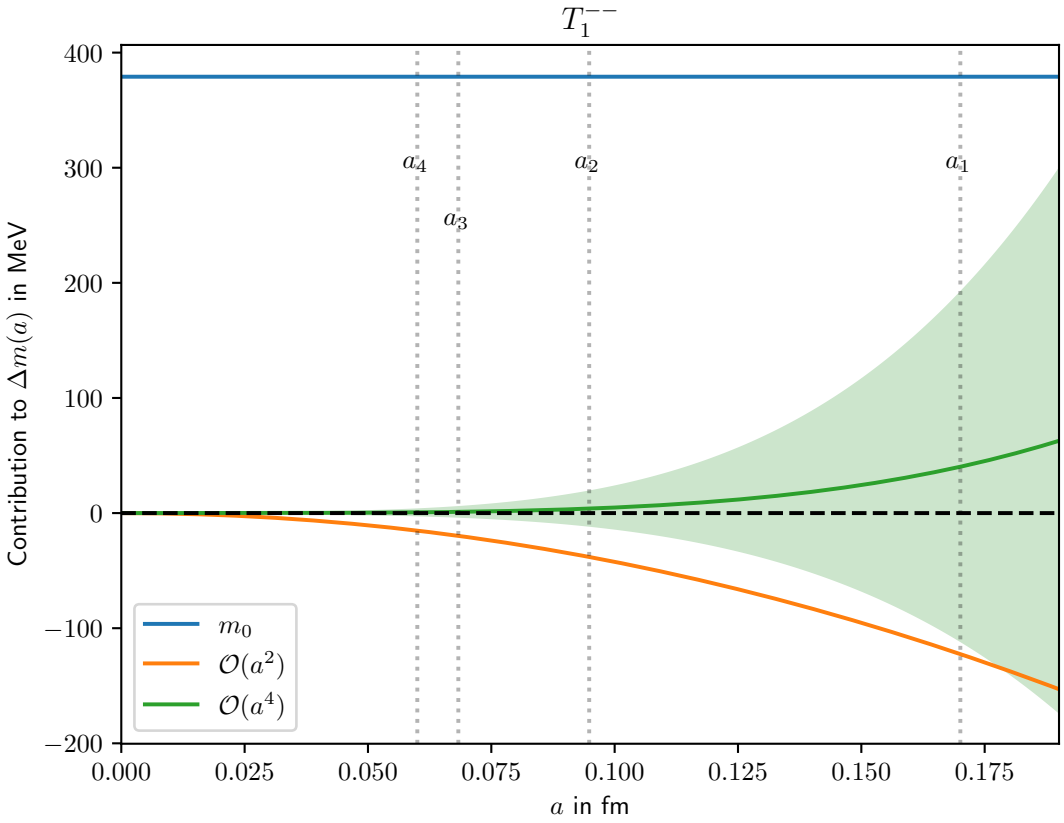

Figure 10: Different terms obtained by fitting the mass splitting data of T_1^{--} and T_1^{+-} [3] via equation (84). The constant (blue) and quadratic (orange) term are shown, for a better visibility, without error bars, while the green curve describes terms of $\mathcal{O}(a^4)$. The lattice spacings a_1, a_2 and a_3 were used in [3], while the computations in this thesis stick to lattice spacings a with $a \leq a_2$.

Ensemble	β	a in fm	$N^3 \times N_T$	N_{or}	N_{therm}	N_{sep}	N_{meas}	$N_{\text{s,opt}}$
A	6.000	0.093	$12^3 \times 26$	4	20000	50	3200	33
B	6.284	0.060	$20^3 \times 40$	12	20000	100	1450	82
C	6.451	0.048	$26^3 \times 50$	15	40000	200	800	123
D	6.594	0.040	$30^3 \times 60$	15	40000	200	800	164

Table 7: Gauge link ensembles [1].

5.2 Optimizing APE-smearing

In this section the number of APE-smearing steps N_s is optimized by examining the effective mass at $\tau = 1$ with $\alpha = 0.5$ for all 20 gluelump states at $\beta = 6.284$. For $m_{\text{eff}}(\tau = 1)$ the impact of higher excitations is not negligible, thus an optimal N_s is characterized by a minimal effective mass at small τ. Figure 11 shows $m_{\text{eff}}(\tau = 1)$ versus the number of smearing steps N_s for a T_1^{--} gluelump. The minimum is achieved at $N_s \approx 51^{+19}_{-12}$, while the errors were chosen such that the error bands overlap. In general, it turned out, that for N_s values larger than the optimal value, the slope is significantly lower than for smaller values. Thus even for $N_s \geq N_{s,\text{opt}}$ the overlap should be sufficient large enough. This procedure has to be repeated for all 20 gluelump operators and leads to figure 12, where the optimal N_s for all $\Lambda^{\mathcal{PC}}$ is shown. Since the error bars, especially the upper border, can get very large, they are not displayed explicitly. It turned out, that an optimal overlap for lighter gluelumps, is achieved with smaller N_s. Since mass spectroscopy is possible for lighter states up to larger times at which excitations are sufficiently suppressed, N_s is primarily optimized for heavier gluelumps, which led to $N_{s,\text{opt}} = 82$ for $\beta = 6.284$. For the other lattice spacings, the optimal smearing steps are given in table 7. They were obtained by choosing the same ratios like in [1] and additionally performing a cross-check for single gluelumps.

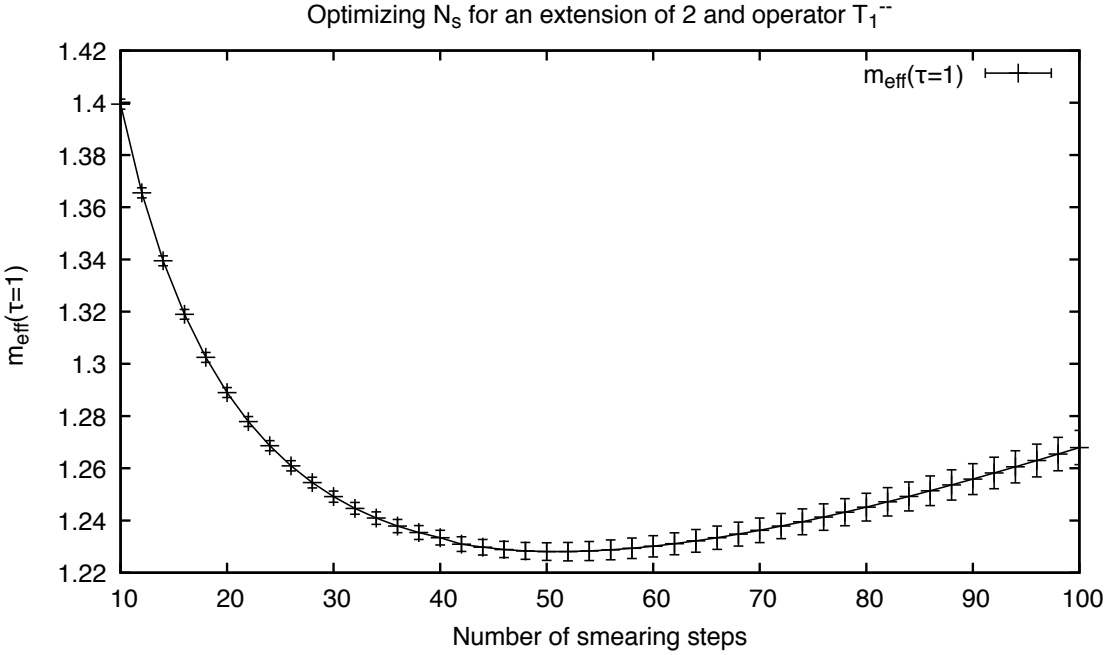

Figure 11: $m_{\text{eff}}(\tau = 1)$ versus the number of smearing steps N_s for T_1^{--}.

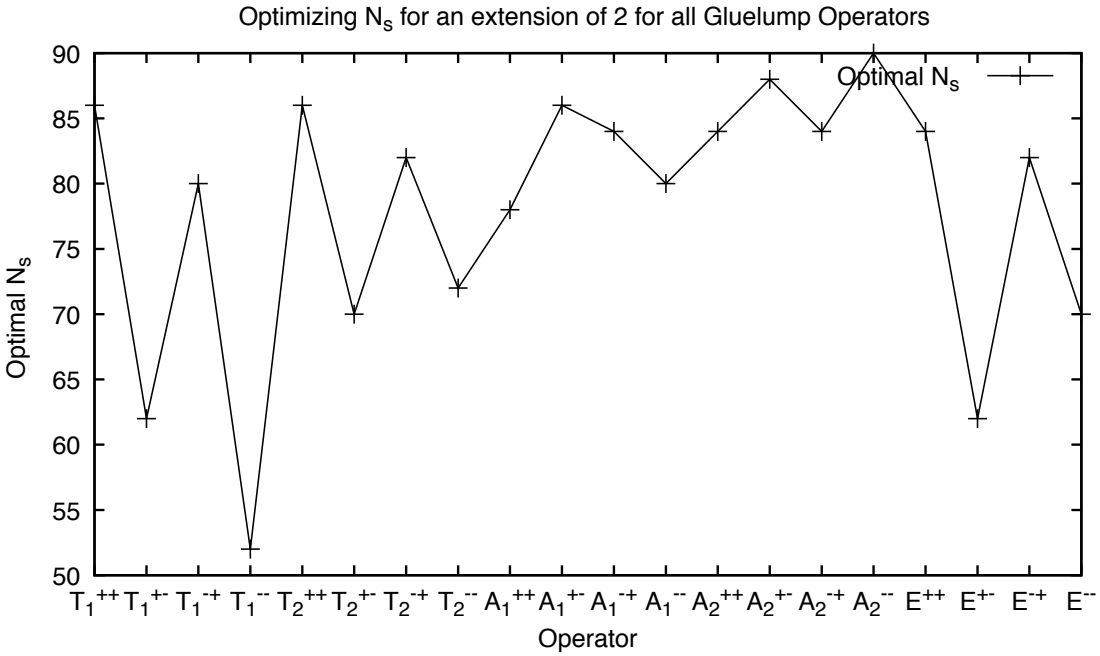

Figure 12: Optimal number of smearing steps N_s for all $\Lambda^{\mathcal{PC}}$.

5.3 Optimizing the multilevel algorithm

The multilevel algorithm is very complex and difficult to optimize due to its many parameters. For a given number of levels, one has to determine the optimal sublattice structure, the number of sweeps between two measurements and the total number of sublattice measurements. Even though the optimal parameters might differ for different lattice spacings, all optimizations could only be performed on non-HYP-smeared gauge fields at $\beta = 6.284$ due to the large computational time consumption.

The purpose of the multilevel algorithm is to reduce fluctuations in the temporal transporters and generate smaller errors σ in the effective mass/correlation function for a given computational time T_{ml}. For statistically independent gauge field configurations $\sigma \propto 1/\sqrt{N}$ is expected and therefore $N \cdot \sigma^2 \propto T_{ml} \cdot \sigma^2 = \text{const}$. This is not the case for the number of sublattice measurements n_m, where a minimum in $n_m \cdot \sigma^2$ at the optimal value for a given t, is expected. The procedure for the optimization of n_m for a given sublattice structure is given as follows:

1. Generate N_{top} top level configurations.
2. Vary the number of sublattice measurements n_m.
3. Find the minimum in $n_m\sigma^2$ for a given t and $\Lambda^{\mathcal{PC}}$.

The final n_m was determined, by performing computations on $N_{\text{top}} = 50$ top-level configurations, for the T_1^{+-} gluelump at $t = 12$, while the errors of the effective mass $m_{\text{eff}}(t)$ were

examined. T_1^{+-} was chosen for optimization since all masses are given relative to its mass, while $t = 12$ turned out to be sufficiently large enough for a positive influence of the multilevel algorithm, but not too large for a proper mass extraction. Exemplary, the above mentioned graph is displayed in figure 13 for two possible operator extensions on a sublattice with thickness $p_i = 2$. The minimum is visible at $n_m = 20$ for both extensions. This is no surprise since both correlators contain the same adjoint temporal transporters and only differ in the linear combination $G(\tau)$, which is not influenced by the multilevel algorithm due to its position on the time-slice boundaries.

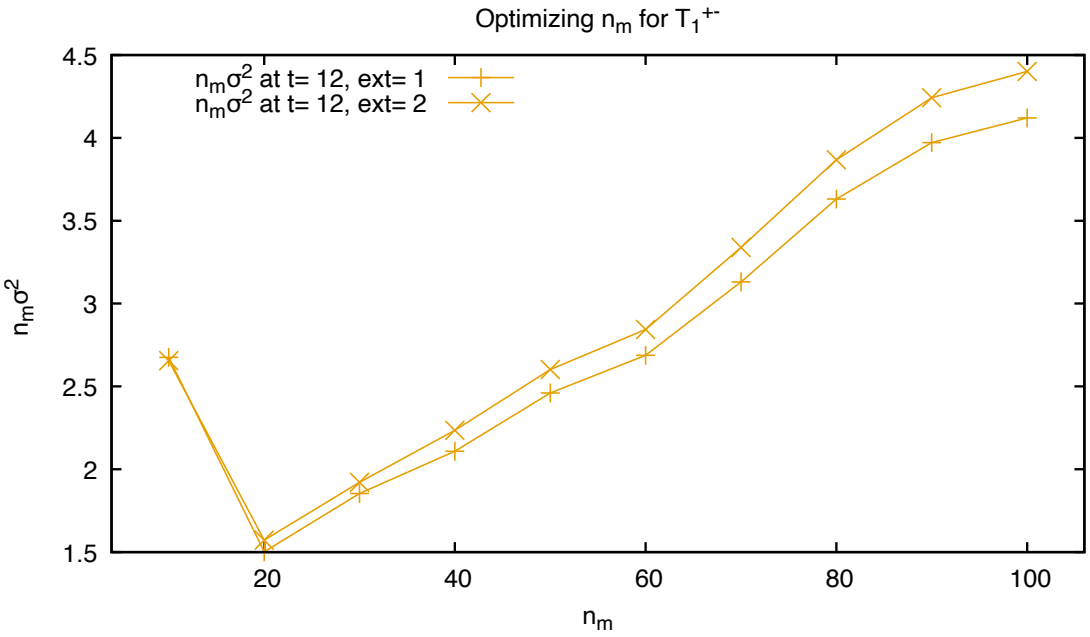

Figure 13: $n_m\sigma^2$ versus n_m for the error of the effective mass of a T_1^{+-} gluelump at $t = 12$ for an extension of one and two on sublattice C (cf. table 8).

Table 8 shows the different sublattice structures used in this work. The number of levels does not include the top lattice. The given structures are periodically repeated until the lattice is filled with time-slices. While the correlation function for the structures A, B and F can be computed for all possible time separations t, C only allows $t = 0, 2, 4, \ldots$. The number of data points is even more restricted for D and E, where just $t = 0, 4, 8, \ldots$ is possible. In contrast, data for G is extracted from different simulations with structures G_i respectively. The last row of table 8 displays which t were computed on every sublattice.
The equidistant partitioned structures A, B, C, D and E are compared in figure 14. It turned out that the use of the multilevel algorithm improves the efficiency in every case. Generating results with the same precision without the algorithm would require 10^2 up to 10^4 times longer calculations (depending on the chosen temporal transporter length). D and E are producing similar results, while $\sigma^2 \cdot T$ is slightly smaller when using two levels. It is necessary to con-

sider that lattices with a larger time-slice thickness reduce the total number of data points. In principle, this can affect the temporal translation invariance and reduce the quality of effective mass fits. Especially for heavier gluelumps, where the mass spectroscopy is in some cases only possible up to $t \approx 6$, time-slices of thickness four are significantly too thick.

Sublattice		No. of levels	Structure 1	Structure 2	$n_{m,1}$	$n_{m,2}$	Used $t \neq 0$
A		0	$\times$	$\times$	$\times$	$\times$	1,2,3,...,20
B		1	$[1,1,1,1,\dots]$	$\times$	10	$\times$	1,2,3,...,20
C		1	$[2,2,2,2,\dots]$	$\times$	20	$\times$	2,4,6,...,20
D		1	$[4,4,4,4,\dots]$	$\times$	100	$\times$	4,8,12,...,20
E		2	$[4,4,4,4,\dots]$	$[2,2,2,2,\dots]$	10	10	4,8,12,...,20
F		1	$[1,2,3,4,\dots]$	$\times$	70	$\times$	1,2,3,...,20
G	G_1	1	$[1,1,1,1,\dots]$	$\times$	10	$\times$	1,2,11,13
	G_2	2	$[3,3,3,3,\dots]$	$[1,2,1,2,\dots]$	10	10	3,6,9
	G_3	2	$[4,4,4,4,\dots]$	$[2,2,2,2,\dots]$	10	10	4,8,12,16
	G_4	2	$[5,5,5,5,\dots]$	$[2,3,2,3,\dots]$	10	10	5,10,15
	G_5	2	$[7,7,7,7,\dots]$	$[3,4,3,4,\dots]$	10	10	7,14

Table 8: Sublattices used in this thesis with given sublattice structure on each level and number of measurements. G is build from several different sublattice structures G_i.

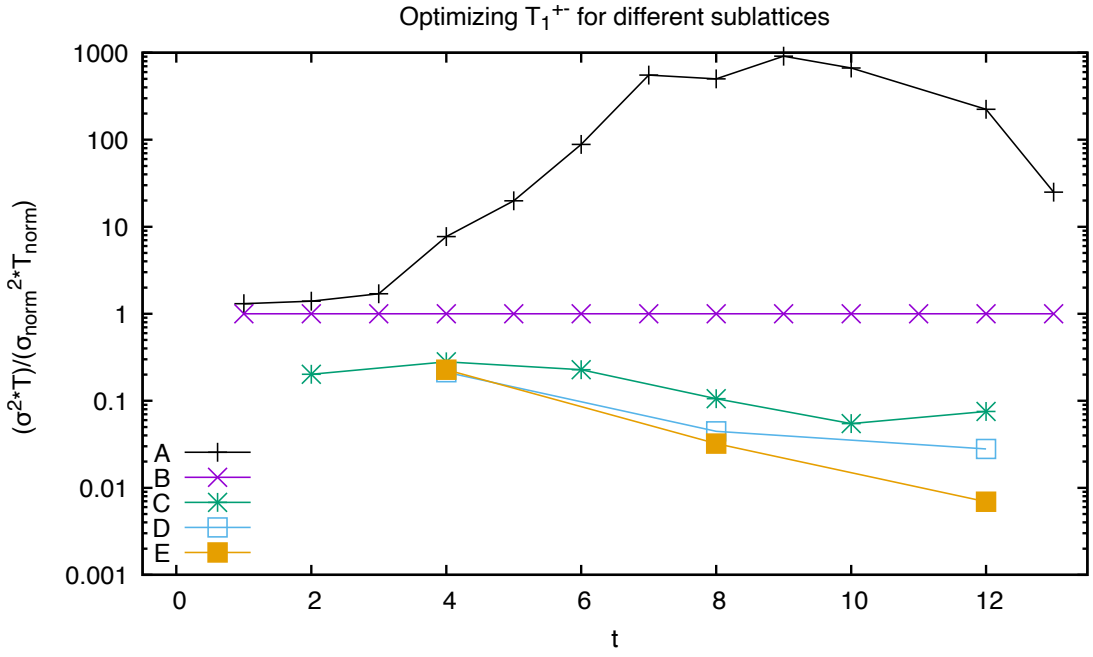

Figure 14: Logarithmic comparison of the efficiency of different sublattice structures (A, B, C, D and E) for several t values. σ is the relative error of the effective mass, T the total computation time, while the subscript *norm* corresponds to sublattice B.

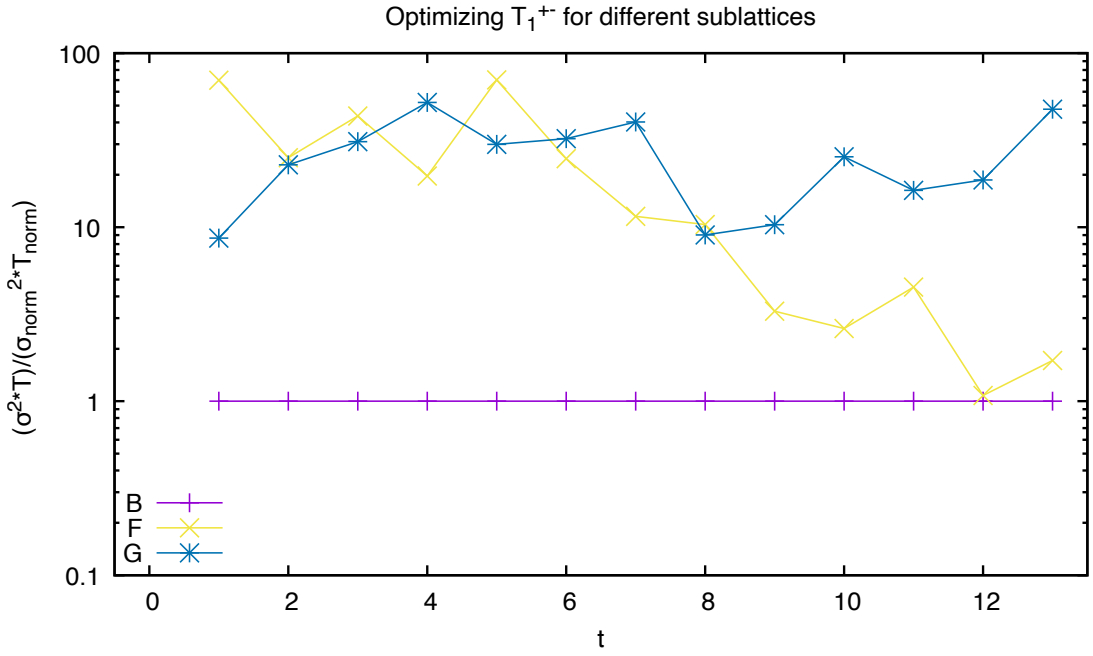

Figure 15: Logarithmic comparison of the efficiency of different sublattice structures (B, F and G) for several t values. σ is the relative error of the effective mass, T the total computation time, while the subscript *norm* corresponds to sublattice B.

The sublattices F and G are trying to combine the efficiency of large time-slice thicknesses with the possibility to compute effective masses for all possible temporal extensions. While F contains time-slices with thicknesses $p_i \neq p_{i+1} \neq p_{i+2} \neq p_{i+3}$, G combines different sublattice structures with thicknesses up to seven. They are compared with B in figure 15.
Both variants do not seem to improve the efficiency for $t \leq 13$. On the one hand, only 10% of the samples are present in F compared to B. Additionally, the computation time is increased approximately by a factor of four. Thus an approximately 40 times higher $\sigma^2 T$ value for small times is expected. With increasing t the positive effects of larger time-slices start to contribute, which leads to better performance. Since for t values larger than thirteen, where F might have better efficiency, no proper mass extraction is possible, variant F is not used.
Sublattice G is a very complex construct and therefore many different factors can contribute to the efficiency. First, the computation time for G is about ten times larger than for B. This explains the behavior of $t = 1$ and 2. One main issue is the prime number temporal lengths since they have to be computed either on G_1, where no large time-slices contribute or on sublattices with thicker time-slices, which reduces the total number of samples and increases the computation time. On a sublattice with partitioning $[1, 1, 1, 1, \dots]$ full temporal translation invariance is achieved since the computation of correlation functions is possible at every lattice site, which is not the case for larger time-slices. Additionally, G is built partly from a structure with odd p_j. The former analysis was only performed on even lattices.

Last but not least some substructures (e.g. G_5), cause about one-quarter of the computation time, but only provide a few additional data points.
Unfortunately, we were unable to construct sublattices, which are more efficient than sublattices with a uniform partitioning. But this does not mean that uniform structures are in general more efficient. A more detailed investigation would exceed the scope of a master thesis.
Both sublattices B and C are possible candidates for the final computation. While C provides a higher efficiency on single mass data points but reduces the total number of samples, B can be applied to any lattice extension. Computations have shown that effective mass fits for B and C of gluelump masses result in similar errors for lighter gluelumps, while for heavier states B is preferable. Therefore, structure B with $n_u = 30$ is used for all final calculations, since it can be applied to any top lattice without further adjustments and increases the efficiency significantly.

5.4 Mass determination

Correlation functions were computed with and without the use of HYP-smearing on four different lattice spacings for twenty different gluelump operators. This leads to a total of 160 different mass spectra. Therefore, it is necessary to use algorithms that generate consistent results for all data sets. Two different approaches are applied, which are based on effective masses and correlation functions respectively. To extract masses and errors the fitting algorithms described in [34] were used, while the errors of $C(t)$ and $m_{\text{eff}}(t)$ were estimated using the jackknife method.

5.4.1 Mass extraction procedures

Procedure *I*: The first procedure is based on the property, that a correlation function is an infinite sum of exponential functions of energy differences (cf. eq. (16)). The correlation function is approximated using the approach

$$C(\Lambda^{\mathcal{PC}}, t) = c_0 \cdot e^{-m_0 t} + c_1 \cdot e^{-m_1 t}. \tag{86}$$

Where $c_0, c_1 > 0$ and $0 \leq m_0 \leq m_1$. If the APE-smearing was successful one would expect $c_1 < c_0$. While m_0 can be interpreted as the mass of the ground state, this is not possible for m_1. The second exponential may be understood as a superposition of the contributions of all higher-lying gluelump states to the correlation function. Fits with more exponential functions turned out to be too unstable.

Procedure *II*: The second algorithm uses effective masses and determines the mass value by identifying the plateau region. It was used previously in [31].
For the mass extraction χ^2-minimizing fits of a constant are applied to $m_{\text{eff}}(\Lambda^{\mathcal{PC}}, t)$ in between t'_{min} and t'_{max}. The fit range is chosen for every data set individually and is determined as follows:

1. t_{min} is the minimal t value, where $m_{\text{eff}}(\Lambda^{\mathcal{PC}}, t)$ and $m_{\text{eff}}(\Lambda^{\mathcal{PC}}, t+a)$ overlap within error bands, i.e. differ less than $\Delta = \sigma_t + \sigma_{t+a}$.

2. t_{max} is defined as the maximal t, where $m_{\text{eff}}(\Lambda^{\mathcal{PC}}, t)$ is computed and the statistical error is reasonably small.

3. Fits are then performed for all ranges $t'_{\text{min}} \leq t \leq t'_{\text{max}}$, where $t_{\text{min}} \leq t'_{\text{min}}$ and $t'_{\text{max}} \leq t_{\text{max}}$ with at least three data points.

4. $m(\Lambda^{\mathcal{PC}})$ is taken as the result of the fit with the longest plateau and $\chi^2/\text{dof} \leq 1$.

The above-described algorithm worked reliably in about 85% of the cases. In the other cases, the fit range had to be varied slightly. For heavier gluelumps a fit with $\chi^2/\text{dof} \leq 1$ was not always achievable and therefore we decided to use the range, where χ^2/dof was minimal.

5.4.2 Mass results

Figure 16 shows one example plot for both mass extraction procedures. The results agree very well within error bands, while the mass extraction of the ground state via procedure *I* suffers from an approximately 30% larger uncertainty. Nevertheless, the behavior of the effective mass for large t, shows the good quality of our data, especially for the magnetic gluelump T_1^{+-}. As for the continuum extrapolation, all masses are given relative to $m(T_1^{+-})$, it is important, that no higher-lying states contribute to the extracted mass. Furthermore figure 17 shows the comparison of the computed gluelump masses at $\beta = 6.451$ for both procedures.
In most cases, the results agree within error bands, while the exponential fit leads mostly to larger errors. In general, all masses derived with the effective mass fit are larger. This could be an indication of a non-negligible contribution of higher-lying states for the chosen t'_{min}. All results for both procedures, lattice spacings and with and without the use of HYP-smearing are collected in Appendix A in the tables 14-17. Additional to the ground state mass, the corresponding errors and χ^2/dof values are displayed. The gluelump spectrum is discussed in detail in section 6, where the gluelump masses are extrapolated to the continuum.

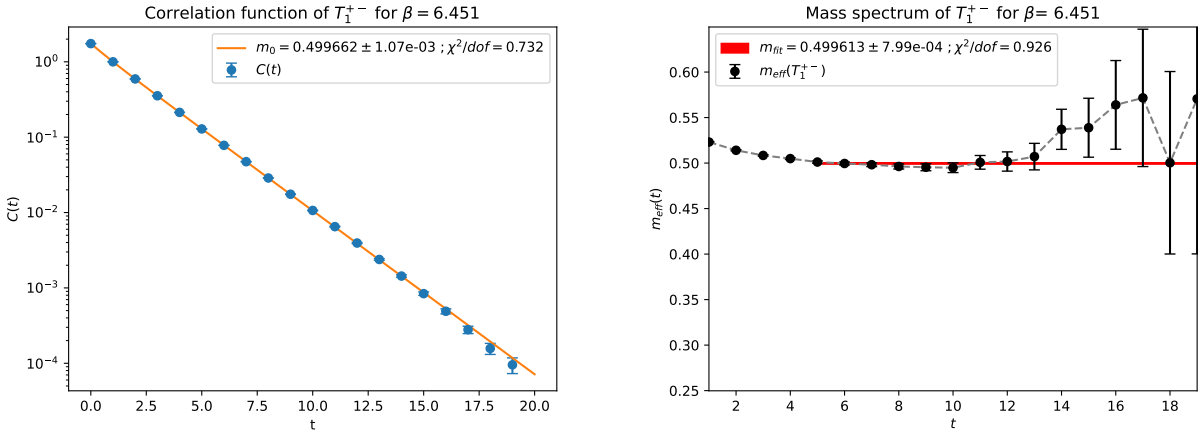

Figure 16: Mass extraction of T_1^{+-} for $\beta = 6.451$ with the use of HYP-smearing for procedure *I* with a logarithmic scale (left) and procedure *II* (right). The results of the fits are marked in orange and red respectively.

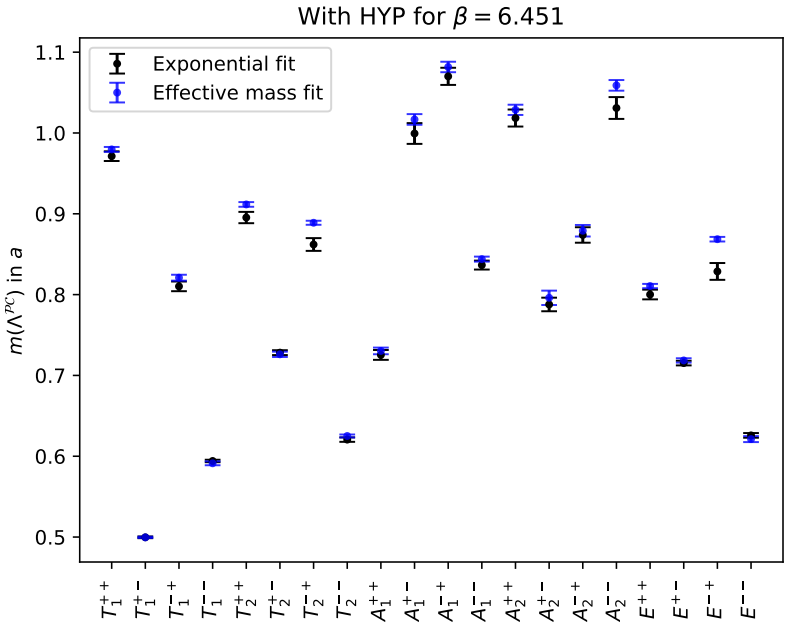

Figure 17: Comparison of the effective mass fit (blue) and the exponential fit (black) for all 20 $\Lambda^{\mathcal{PC}}$ gluelumps at $\beta = 6.451$.

5.4.3 Hybrid potentials

The aim of this section is to compare the derived masses for T_1^{+-} with the bare lattice data of the hybrid static potentials computed in [1]. According to equation (22) and table 1 the potentials Σ_u^- and Π_u should approach $m(1^{+-})$ for $r \to 0$. For this reason, we have to be sure, that $m(T_1^{+-}) = m(1^{+-})$ is correct. On the one hand, a computation of the corresponding mass was possible on all used lattice spacings in wide plateau regions, which indicates that no heavier states contribute. On the other hand the possible two lowest-lying spin states in T_1^{+-} are $J = 1$ and 3, while for A_2^{+-} $J = 3, 6, 7 \ldots$ is possible (cf. table 4). If $m(T_1^{+-}) = m(3^{+-})$ would hold, $m(T_1^{+-}) \approx m(A_2^{+-})$ is expected, which is not the case. Thus we conclude that $m(T_1^{+-}) = m(1^{+-})$ is correct.
In figure 18 the comparison of the hybrid statice potentials and gluelump masses are displayed. Taking the gluelump masses into account, all results with non-HYP-smeared links, show a similar upward curvature for $r \to 0$. This behavior agrees with the expected repulsive behavior in pNRQCD for small r [12]. Unfortunately, the potentials were only computed for $r \geq 2a$. A data point at $r = a$ would, especially for $\beta = 6.594$, provide deeper insights in the agreement of the mass results with the potentials for $r \to 0$. Nevertheless our masses confirm qualitatively equation (22) and the pNRQCD prediction.

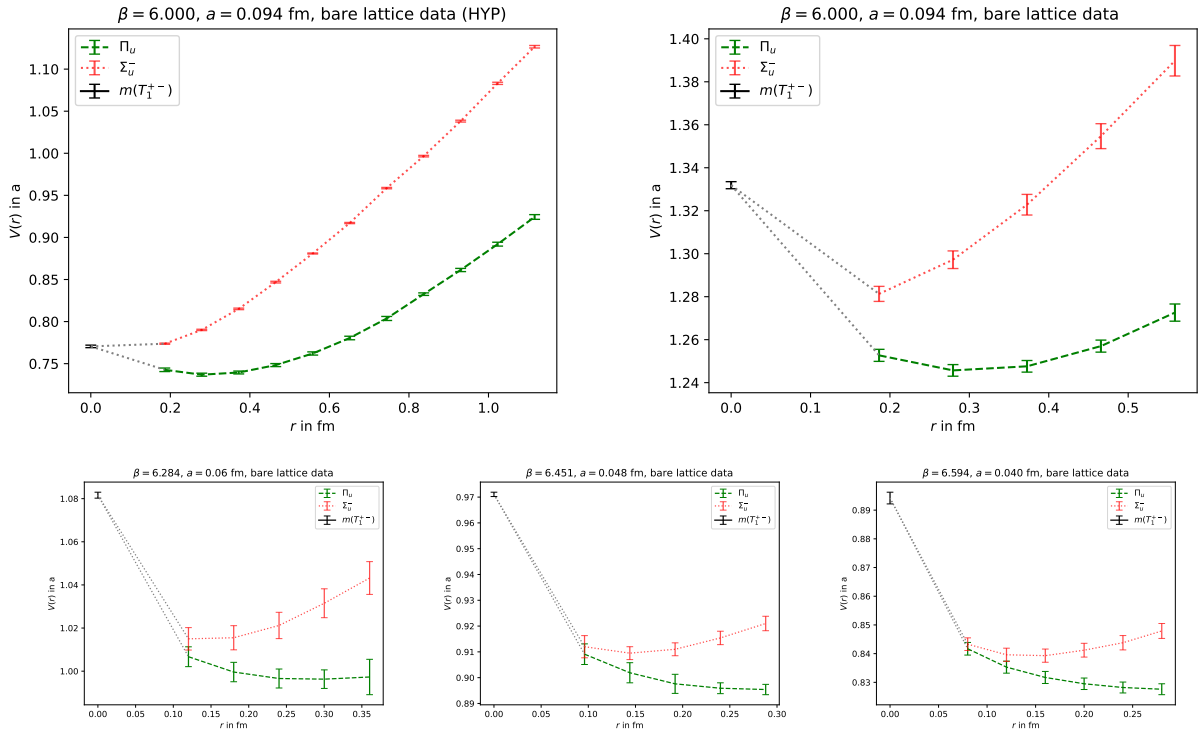

Figure 18: Comparison of the Σ_u^- and Π_u potentials computed in [1] with the mass of the lightest gluelump T_1^{+-} versus the separation distance r in fm. Additional to the potentials without the use of HYP-smearing, the results for HYP-smeared gauge fields are displayed in the upper left corner. All potentials/masses are given in units of the lattice spacing.

By comparing the upper left and upper right plot in figure 18 a clear mismatch for HYP-smeared gauge field configurations is present, where no upward curvature is visible for $r \to 0$. According to reference [3] the self-energy at $r \neq 0$ can be considered as $2E_F$, while at $r = 0$ it is given by $E_A = 9E_F/4$. Thus the self-energy is $\frac{9}{8}$ times larger at $r = 0$. This mismatch is a first indication for the behavior for $r \to 0$. By comparing the smeared and unsmeared bare potential lattice data at $r = 6a$, an energy difference $\Delta E_{\text{hybrid}} = 0.509(8)$ is obtained, while examining the difference for $m(T_1^{+-})$ leads to $\Delta E_{\text{gluelump}} = 0.561(4)$. Even within error bands both self-energy reductions do not agree. Shifting the gluelump mass in the smeared spectrum by $(\Delta E_{\text{gluelump}} - \Delta E_{\text{hybrid}})$ would then recreate the expected curvature. Additional $\Delta E_{\text{gluelump}} \approx 9/8 \Delta E_{\text{hybrid}}$ holds, which agrees with the above relation between E_A and E_F and would indicate that HYP-smearing reduces the self-energy proportionally.
Hence we conclude that bare lattice data for HYP-smeared potentials and gluelump masses cannot be compared without any further adjustments.

5.4.4 Overlap and possible glueball mass determination

One advantage of procedure I for mass extraction is, that the fit parameters c_0 and c_1 can give an insight into, whether APE-smearing was successful. Although c_1 cannot be interpreted as the overlap of the next higher-lying state, but as a superposition of several heavier states, $c_0 \gg c_1$ can indicate that the smearing was successful. In figure 19 the fraction $|c_1|/|c_0|$ at $\beta = 6.594$ for all twenty computed gluelump masses is shown. Smaller fractions correspond to higher overlaps with the ground state. Note that for all β the behavior is similar and thus only values for $\beta = 6.594$ are drawn. In most cases $|c_1|/|c_0| \lesssim 0.35$ was achieved. Together with faster decreasing exponential functions of heavier states, a ground state mass extraction even at small times is therefore possible. The smallest overlaps occur for A_2^{+-} and A_2^{--}, which may correspond to a general bad overlap of the state created by the chosen operator with these states. Especially A_2^{+-} and A_2^{--} masses determined by an effective mass fit should therefore be considered with caution.

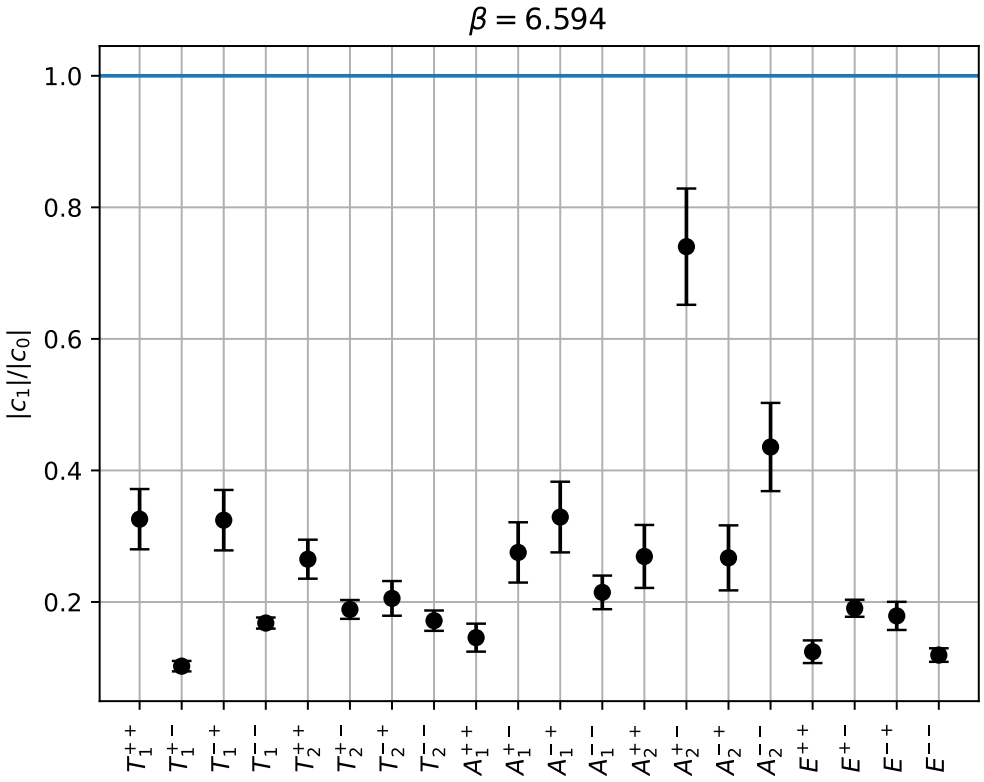

Figure 19: Fraction of the prefactors c_1 and c_0, which were obtained by fitting the function, given in equation (86) to the HYP-smeared correlation data for all 20 $\Lambda^{\mathcal{PC}}$ gluelumps at $\beta = 6.594$. $|c_1| = |c_2|$ is marked in blue.

The gluelump correlation function (cf. eq. (44)) is consisting of two terms. While both terms contain the linear combinations of closed link loops $G(\tau)$, only the first term includes temporal links. As mentioned before the symmetry group on the lattice for glueballs and gluelumps is the cubic group. Therefore, corresponding creation operators might be build from the same $G(\tau)$. According to [35] a possible correlation function for glueballs is given by

$$C(\tau_2 - \tau_1) = \mathrm{Tr}(G(\tau_2)^\dagger)\,\mathrm{Tr}(G(\tau_1)), \tag{87}$$

where all quantities are again defined at the same spatial lattice site. In the case of A_1^{++}, one has to additionally subtract the vacuum contribution. Since the quantity given in equation (87) appears in the gluelump correlator as well, one might expect that it is possible to extract glueball masses on the fly, while computing the gluelump spectrum. Unfortunately, this is not possible because of the following reasons:
On the one hand, the chair-shaped operators, used in this thesis, are considered as "bad" glueball operators in [36], since they suffer from a bad signal-to-noise ratio. On the other hand, the total number of APE-smearing steps was adjusted, such that the effective mass of gluelumps at small times was minimized. This probably causes a worse overlap to glueball states. Additionally, the applied HYP-smearing and multilevel algorithm do not improve possible glueball results.
Hence, a precise computation of glueball masses would require another set of operators, for this purpose adjusted smearing step sizes and if necessary the application of different numerical procedures, like for instance *blocking*. An attempt to neglect the "glueball contribution" in the gluelump correlator neither reduced the computation time significantly nor increased the signal-to-noise ratio.

6 Continuum gluelump masses

As previously discussed, gluelump masses contain an unphysical self-energy, which is divergent for $a \to 0$. Therefore, only mass differences can be extrapolated to the continuum without any further adjustment. In agreement with section 5.1 a χ^2-minimizing fit is performed to

$$m(\Lambda^{\mathcal{PC}}) - m(T_1^{+-}) = m_0 + c_2 \cdot a^2 \quad ; \quad \Lambda^{\mathcal{PC}} \neq T_1^{+-}. \tag{88}$$

The errors of $m(T_1^{+-})$ and $m(\Lambda^{\mathcal{PC}})$ are added linearly since they are not statistically independent, while the corresponding χ^2-minimizing fit is performed with the methods described in reference [34]. The continuum masses are then given by the fit constant m_0. Figure 20 shows four examples for the continuum extrapolation. The mass splittings have a clear a^2-dependence, which makes us confident, that equation (88) was a good ansatz.

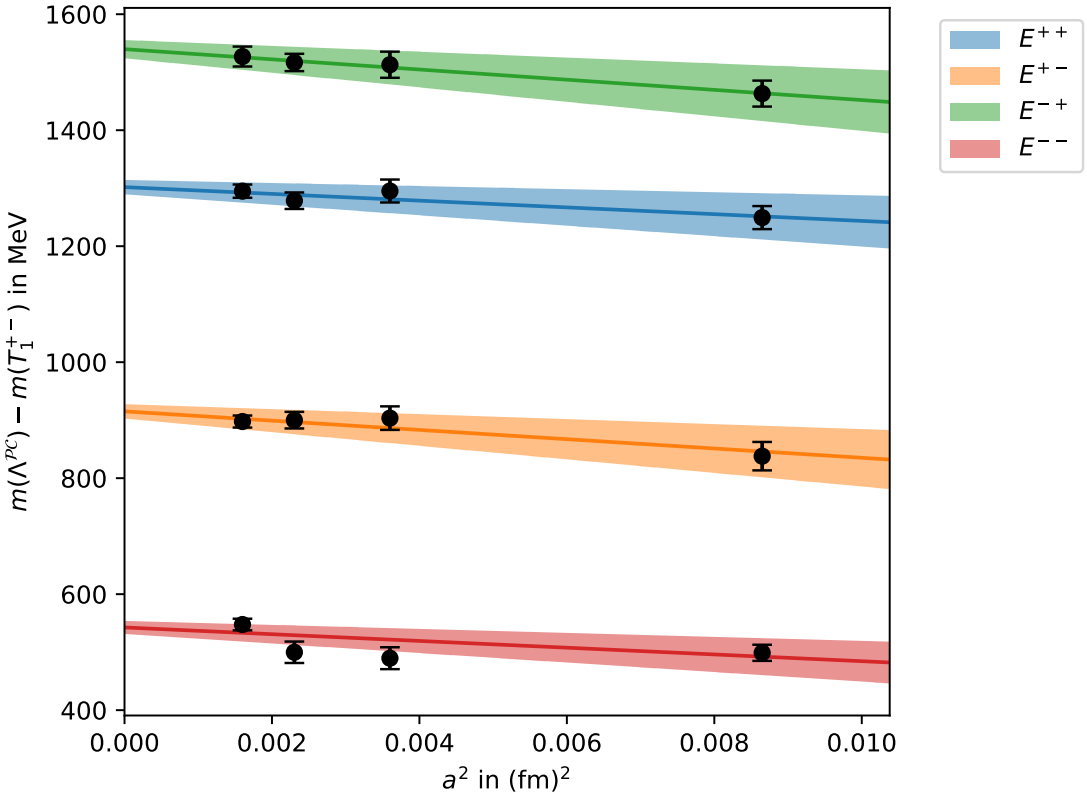

Figure 20: The mass splittings of the E representation for all possible $\mathcal{PC}$ states in MeV versus the squared lattice spacing in fm^2. Single data points are marked in black, while the continuum extrapolation via fitting equation (88) to the data points, including error bands, is colorized with the color given in the legend. The mass points were extracted using procedure I with the use of HYP-smearing.

The mass splittings for all 19 gluelumps are given in table 9 with corresponding errors and χ^2/dof values, which makes it possible to compare the different procedures and if the use of HYP-smearing provides an improvement. Similar to the results at a given lattice spacing, the mass results are in the same range for both procedures and agree in most cases within error bands. The largest mismatch appears, like previously predicted, for A_2^{+-} and A_2^{--}. Probably procedure I provides better results here since states of higher masses seem to contribute significantly to the effective mass in the extraction time range.
The application of HYP-smearing reduced the average error of the masses computed via procedure I by 5MeV and 10MeV for procedure II, while most masses agree within error bands. For one of the heaviest states A_2^{--}, a large discrepancy between both results is present, which is likely due to the increment of "good" data points for HYP-smeared correlators. In general, the number of effective mass points, where the errors were sufficiently small, was increased. Thus we are sure that $m_{\mathrm{I,HYP}}$ and $m_{\mathrm{II,HYP}}$ are more probable correct and therefore the following discussion is performed for them.

$\Lambda^{\mathcal{PC}}$	m_{I}	χ^2/dof	m_{II}	χ^2/dof	$m_{\mathrm{I,HYP}}$	χ^2/dof	$m_{\mathrm{II,\,HYP}}$	χ^2/dof
T_1^{++}	1920(40)	1.47	1985(20)	2.60	1924(30)	1.52	1977(27)	5.98
T_1^{-+}	1278(29)	0.83	1329(21)	0.31	1288(27)	0.09	1351(14)	2.25
T_1^{--}	382(11)	1.69	393(17)	0.45	386(9)	1.86	359(9)	1.44
T_2^{++}	1734(29)	2.31	1762(18)	1.66	1731(27)	1.90	1742(16)	0.83
T_2^{+-}	968(16)	0.89	975(18)	0.62	973(15)	0.13	951(15)	0.23
T_2^{-+}	1594(29)	2.67	1640(17)	0.50	1604(28)	2.06	1629(17)	0.88
T_2^{--}	503(15)	0.45	517(13)	0.54	511(13)	0.57	505(9)	0.15
A_1^{++}	996(24)	2.92	1005(18)	1.60	1006(23)	1.73	997(15)	0.92
A_1^{+-}	2180(60)	1.34	2220(40)	2.18	2210(60)	1.52	2261(26)	3.07
A_1^{-+}	2420(60)	0.12	2460(40)	0.78	2420(50)	0.32	2442(25)	0.81
A_1^{--}	1390(27)	0.33	1429(19)	0.10	1396(25)	1.20	1410(16)	2.57
A_2^{++}	2150(50)	1.01	2153(29)	0.43	2150(50)	0.79	2125(29)	2.75
A_2^{+-}	1240(40)	1.99	1310(25)	0.99	1200(40)	0.79	1280(29)	1.44
A_2^{-+}	1530(50)	0.44	1550(40)	0.08	1560(40)	0.64	1584(22)	0.93
A_2^{--}	920(14)	3.20	1090(12)	5.17	2320(60)	0.93	2340(40)	0.51
E^{++}	1313(25)	1.21	1300(18)	0.53	1306(23)	1.39	1302(13)	0.53
E^{+-}	894(16)	0.44	888(23)	0.07	902(15)	0.31	915(13)	0.54
E^{-+}	1541(29)	5.70	1550(19)	0.92	1541(27)	6.02	1540(16)	0.04
E^{--}	551(14)	3.26	544(17)	4.81	560(13)	2.09	543(12)	3.84

Table 9: Continuum results of $m(\Lambda^{\mathcal{PC}}) - m(T_1^{+-})$ with χ^2/dof values for all 19 possible mass differences in MeV. The subscripts I and II denote the used procedure for the mass extraction, while HYP indicates, that HYP-smearing was applied.

6.1 Spin identification

Every irreducible representation can contain several different spin states. With the full $\Lambda^{\mathcal{PC}}$ spectrum a possible spin identification/estimation of severals $J^{\mathcal{PC}}$ states is possible. The identifications in the different $\mathcal{PC}$ sectors are performed with figures 21, 22 and table 4. Please note that the following discussion is based on the computed masses and is not generally applicable to $\Lambda^{\mathcal{PC}}$ from different computations. Another set of operator shapes can correspond to a different spin identification for a given $\Lambda^{\mathcal{PC}}$.

$\mathcal{PC} = +-$ sector: The masses of T_2^{+-} and E^{+-} agree within error bands. Since both contain $J = 2$ as the lowest spin, one can identify them as 2^{+-}. The next higher-lying states are $J = 3$ and $J = 4$ respectively, thus we conclude that 3^{+-} and 4^{+-} are heavier than 2^{+-}. T_1^{+-} is lighter than all other computed states in this sector, which corresponds to $m(T_1^{+-}) = m(1^{+-})$. A_1^{+-} might be identified as 0^{+-}, but also 4^{+-}, $6^{+-}\ldots$ is possible. A_2^{+-} cannot be associated with $J = 6$, because $m(A_2^{+-})$ is smaller than $m(A_1^{+-})$ and one might expect an influence in the spectrum of A_1^{+-}, where $J = 6$ is included as well. Hence the most probable possibility is $m(A_2^{+-}) = m(3^{+-})$.

$\mathcal{PC} = -+$ sector: For the same reasons like in the $\mathcal{PC} = +-$ sector we can identify $m(T_1^{-+})$ as $m(1^{-+})$. The masses of E, T_2 and A_2 are very close to each other, while the lowest spin level that they all share is $J = 6$. Therefore, it is more probable that $m(2^{-+}) \approx m(3^{-+})$. Hence E^{-+} can be identified as 2^{-+}, while T_2^{-+} and A_2^{-+} might correspond to 3^{-+}. For A_1 again no clear identification is possible.

$\mathcal{PC} = --$ sector: Analogously T_1^{--} is identified as a spin-one state, while E^{--} and T_2^{--} correspond to $J = 2$. Since A_1^{--} and A_2^{--} are separated from all other measured data points by approximately 1000 MeV no clear spin assignment is possible.

$\mathcal{PC} = ++$ sector: A_1^{++} is the lowest-lying state in this sector and is identified as 0^{++}. The next larger spin is $J = 4$, which can be contained in E, T_1 and T_2 as well. Since none of these states are close to A_1^{++}, an assignment with the lowest spin content is most likely. For the first time, a larger mass gap between E and T_2 is visible, consequently, no identification with $J = 2$ is possible for both at the same time. One possible way is to assume that $E^{++} = 2^{++}$ holds, which then results in an assignment of $J = 3, 4, 5\ldots$ for T_2^{++}. An identification of T_1^{++} with 1^{++} is doubtful, since it shares as well $J = 3, 4, 5\ldots$ spin contents with T_2 and the measured mass is heavier. The spin of the measured T_1^{++} mass can thus be assumed to be larger than the spin of T_2^{++}, which then results in $J = 4, 5\ldots$ depending on the chosen angular momentum for T_2^{++}. Last but not least the two lowest possible J for A_2^{++} are 3 and 6. If the previous reasoning is correct the correspondent spin has to be at least 6.

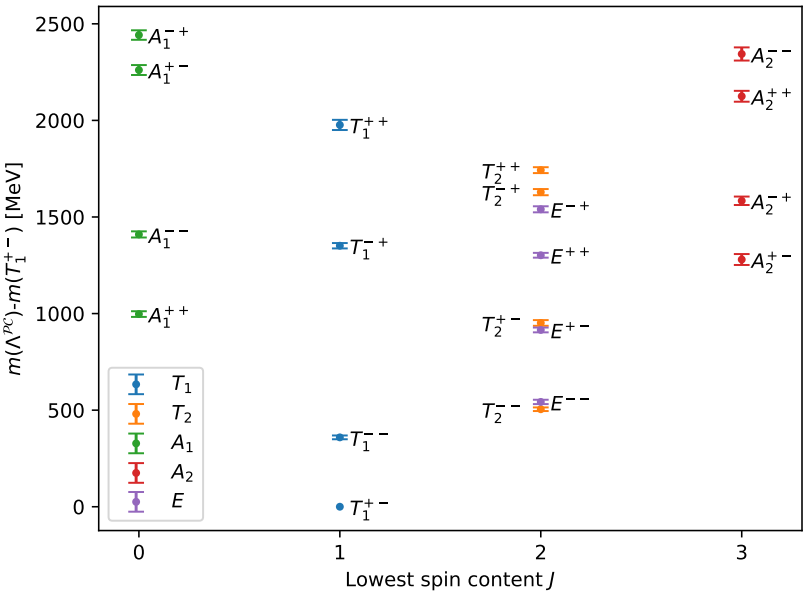

Figure 21: Continuum mass splittings $m_{\mathrm{II,HYP}}$ in MeV versus the lowest possible spin content in each representation. For completeness T_1^{+-} is shown as well.

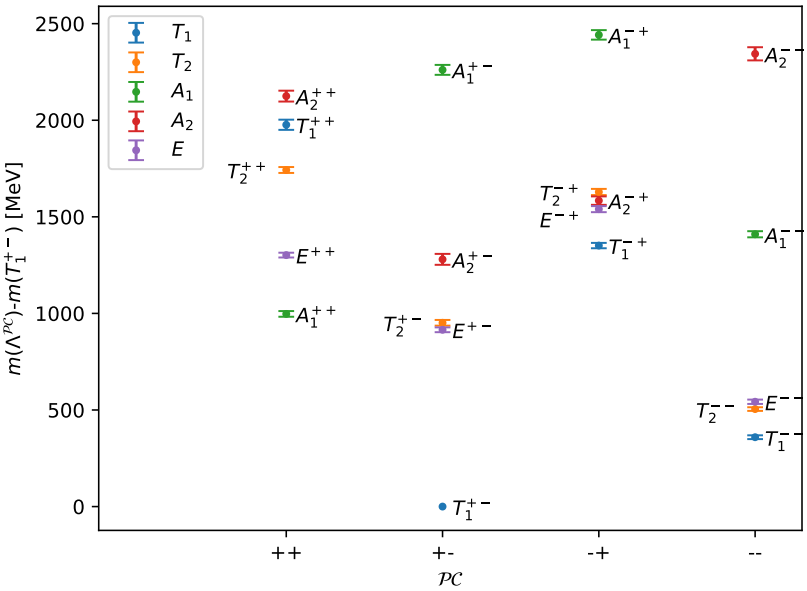

Figure 22: Continuum mass splittings $m_{\mathrm{II,HYP}}$ in MeV for the different $\mathcal{PC}$ channels. For completeness T_1^{+-} is shown as well.

In table 10 the correspondent results are shown and additionally compared with the continuum extrapolation derived in [3]. The errors and in general the literature results have to be taken with caution. According to the authors, the low number of used gauge field configurations might have led to an underestimation of the statistical errors. On the one hand the continuum masses of 0^{++} and 3^{+-} were computed with $\beta = 5.7$ gauge fields, where only one single effective mass could be determined. On the other hand, effective masses were only computed up to $t = 4$. Thus the results might suffer from much larger error bands. Taking this in mind, a good agreement between both results is found. Only the mass of 3^{+-} is significantly smaller in [3], probably due to the use of gauge field with $\beta = 5.7$, where lattice discretization error larger than $\mathcal{O}(a^2)$ contribute, which could in principle lead to a false continuum extrapolation. A comparison with the literature results for each lattice spacing is difficult since the chosen gauge field couplings except for $\beta = 6.0$ differ in both works. For $\beta = 6.0$ the number of effective mass points was increased by a factor of two up to three, depending on the chosen gluelump. Besides that, the precision was enhanced for each mass point. This leads to better fit results, with smaller χ^2/dof values.

Surprisingly, several states are lighter than the lightest measured spin-zero state 0^{++}. In general, the spectrum does not show any patterns that suggest that states with certain $J^{\mathcal{PC}}$ are heavier. This could be either an indication for missing states in between and a corresponding false spin identification or that the gluelump spectrum does not follow any ordering rules. The performed spin identification was based on the assumption, that in a given irreducible representation, states with larger spins are indeed heavier. In order to show that even this assumption can distort the spin spectrum, in the following the $\mathcal{PC} = --$ sector with the property that states with higher spin are generally heavier, is considered:

For A_1^{--} an assignment as 0^{--} would then be impossible, since $m(1^{--}) \leq m(A_1^{--})$. The corresponding angular momentum has then to be at least four, resulting in the spin of A_2^{--} being at least six. This would, on the one hand, correspond to $m(3^{--}) \leq m(A_1^{--}) \leq m(5^{--}) \leq m(A_2^{--})$. On the other hand, this suggests the existence of a state with 0^{--} lighter than 1^{--}.

In summary, the spin identification with only one set of operators is in most cases more a qualitative interpretation than a precise assignment. A possible way to solve this problem is by choosing a wide range of different operator shapes and solving the *generalized eigenvalue problem* (cf. for instance reference [37]). Analogously to the identification of $J = 2$ states by overlapping computed masses in the T_2 and E representation, certain spin states can be identified by their appearance in different representations.

$J^{\mathcal{PC}}$	Other J	$m_{\mathrm{I,HYP}}$	$m_{\mathrm{II,HYP}}$	m_{lit} [3]
1^{--}		386(9)	359(9)	368(7)
2^{--}		540(40)	530(30)	584(10)
2^{+-}		940(50)	930(30)	970(40)
0^{++}		1006(23)	997(15)	1090(30)
3^{+-}		1200(40)	1280(29)	972(24)
1^{-+}		1288(27)	1351(14)	
2^{++}		1306(23)	1302(13)	
0^{--}	4,6,8...	1396(25)	1410(16)	
2^{-+}		1541(27)	1540(16)	
3^{-+}		1580(60)	1610(50)	
3^{++}	4,5,6...	1731(27)	1742(16)	
4^{++}	5,6,7...	1924(30)	1977(27)	
6^{++}	7,9,10...	2150(50)	2125(29)	
0^{+-}	4,6,8...	2210(60)	2261(26)	
3^{--}	6,7,9...	2320(60)	2340(40)	
0^{-+}	4,6,8...	2420(50)	2424(25)	

Table 10: Most probable spin identifications for mass splittings relative to $m(T_1^{+-})$ in MeV derived applying procedure I and procedure II. In the case that two different states, corresponded to a given $J^{\mathcal{PC}}$, the average was taken, while the error bands were taken from the lower border of the lighter state to the higher border of the heavier state. Additional, in unclear cases other possible spins J are listed, while the last row shows literature values taken from [3].

6.2 Subtraction of the self-energy

Previously only mass differences were extrapolated to the continuum. This section aims to subtract the divergent self-energy, to compute the mass of the lowest-lying gluelump T_1^{+-}. For this purpose, two different approaches are chosen. First of all the self-energy is subtracted by approximating the shape of gluelump masses depending on the lattice spacing a. Secondly, the gluelump masses are converted into the RS-scheme, as it was done in [13]. In the latter case, only computations for $m_{\mathrm{II}}(T_1^{+-})$ are shown, since T_1^{+-} masses extracted with both procedures are almost equal.

6.2.1 Approach I

The divergent self-energy is, according to [29], proportional to $1/(\beta a)$. Additionally, previous computations show, that approximating the discretization errors as $\mathcal{O}(a^2)$ is valid. The mass of the i'th gluelump in the dependence of the lattice spacing might then be approximated as

$$m^{(i)}(a) = c_{\mathrm{self}} \cdot \frac{1}{\beta a} + m_0^{(i)} + c_2^{(i)} \cdot a^2 \quad ; \quad i \in \Lambda^{\mathcal{PC}}. \tag{89}$$

Note that c_{self} is identical for every gluelump, while $m_0^{(i)}$ and $c_2^{(i)}$ differ. Although in general the mass of i'th gluelump is given as $m_0^{(i)}$, only the mass of the lowest-lying gluelump is extracted via this approach. The results are shown in table 11.

Label	$m_0^{(T_1^{+-})}$ in MeV	c_{self} in MeV·fm
I	1727(27)	717(8)
II	1708(30)	726(8)
I,HYP	1218(21)	265(5)
II,HYP	1286(25)	246(6)

Table 11: Results for c_{self} and $m_0^{(T_1^{+-})}$. The same labels for the results as in the previous sections are used.

The mass splitting results in table 9 have then to be shifted by the computed constants. Interestingly, in the case of the application of HYP-smearing, not only the diverging contribution of the self-energy is reduced, but also $m_0^{(T_1^{+-})}$.

6.2.2 Approach II: RS scheme

The form of the short distance hybrid potential $E_n(r)$ in [12] is given by

$$E_n(r) = V_{\rm o}^{\rm RS}(\nu_f) + \Lambda_{\rm H}^{\rm RS}(\nu_f) + b_n r^2. \tag{90}$$

Where $V_{\rm o}^{\rm RS}(\nu_f)$ denotes the octet potential and $\Lambda_{\rm H}^{\rm RS}(\nu_f)$ is the mass of a suiting gluelump (cf. table 1). Hence the gluelump mass appears as an additional constant in the small distance description of hybrid potentials and therefore determines the energy scale setting. A possible way of converting gluelump masses in the RS scheme is given in [13]. The authors related the lattice mass of an arbitrary gluelump $\Lambda_{\rm H}^{L}(a)$ with the gluelump mass in the RS scheme $\Lambda_{\rm H}^{\rm RS}(\nu_f)$. The index H labels different kinds of gluelumps. The lattice mass is connected with the mass in the RS scheme via the following master formula:

$$\Lambda_{\rm H}^{\rm RS}(\nu_f) = \Lambda_{\rm H}^{L}(a) - \left\{\delta\Lambda_{\rm H}^{L}(a) + \delta\Lambda_{\rm H}^{\rm RS}(\nu_f)\right\} \tag{91}$$

As equation (91) implies, $\Lambda_{\rm H}^{\rm RS}$ has a ν_f dependence, which could be, according to [13], interpreted in pNRQCD as a matching scale between ultrasoft and soft physics. In the following $\nu_f = 1\text{GeV}$ is used. The correction in equation (91) reads as

$$\begin{aligned}
\delta\Lambda_{\rm H}^{L}(a) + \delta\Lambda_{\rm H}^{\rm RS}(\nu_f) = {} & \frac{C_A}{2} a^{-1} v_1 \alpha_s(\nu) \\
& + \left\{ \frac{C_A}{2(4\pi)} a^{-1} \left\{ v_2 + v_1[-b_1 + \beta_0 \ln(\nu a)] \right\} + \nu_f \left(\tilde{V}_{s,1} - \tilde{V}_{o,1} \right) \right\} \alpha_s^2(\nu) \\
& + \left\{ \frac{C_A}{2(4\pi)^2} a^{-1} \left\{ v_3 + 2v_2 B_1(\nu a) + v_1[B_2(\nu a) + B_1^2(\nu a) + b_1^2] \right\} \right. \\
& \left. + \frac{\nu_f}{2} \left[2(\tilde{V}_{s,2} - \tilde{V}_{o,2}) - 2(\tilde{V}_{s,1} - \tilde{V}_{o,1}) \frac{\beta_0}{\pi} \ln\left(\frac{\nu_f}{\nu}\right) \right] \right\} \alpha_s^3(\nu) + \dots \ ,
\end{aligned} \tag{92}$$

where

$$B_i(x) = -b_i + 2\beta_{i-1} \ln(x), \quad i = 1, 2.$$

Equation (92) is an NNNLO expansion in α_s. The expansion of $\mathcal{O}(\alpha_s^3)$ is correct up to effects of $\mathcal{O}(1/N_c^2)$[3]. The correspondent coefficients with a short explanation are given in table 12. For the extraction of $\Lambda_B^{\rm RS}(\nu_f)$, $\nu = 1/a = \nu_f$ were used. ν and ν_f do not have to be necessary taken similar, but large logarithms are avoided this way. Values for α_s are interpolated for the used β with the data taken from [38]. In the following the index B refers to the magnetic gluelump T_1^{+-}.

[3] $\mathrm{SU}(3) \to N_c = 3$.

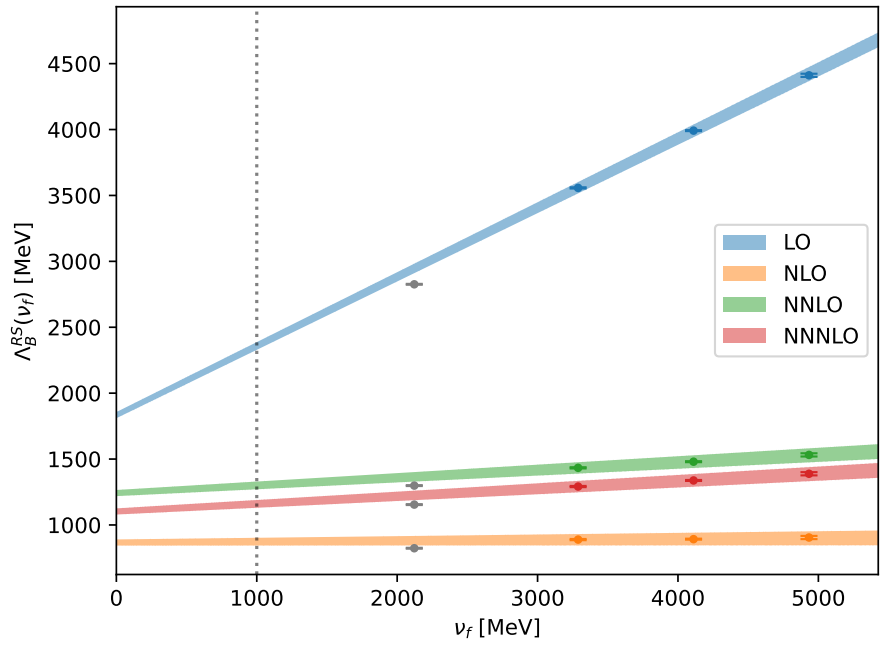

Figure 23: $\Lambda_B^{\mathrm{RS}}(\nu_f)$ for different lattice spacing and fitting orders. Values evaluated at $\beta = 6.0$ (in gray) are not taken into account, due to the non-negligible discretization errors of $\mathcal{O}(a^2)$.

The computation of $\Lambda_B^{\mathrm{RS}}(\nu_f)$ at a given scale consists of the following steps:

1. Convert $\Lambda_B^L(a)$ to $\Lambda_B^{\mathrm{RS}}(\nu_f)$ via eq. (91) with $\nu_f = 1/a$ for all lattice spacings.
2. Perform a linear fit to the dataset $[\nu_f^{(i)}, \Lambda_B^{\mathrm{RS}}(\nu_f)^{(i)}]$.
3. Extract $\Lambda_B^{\mathrm{RS}}(\nu_f)$ at a given ν_f with the above derived linear fit.
4. Estimate the errors of the expansion.

In figure 23 the data for four different expansion orders are shown. Here LO implies that the bare lattice data was used, while NNNLO indicates that terms up to $\mathcal{O}(\alpha_s^3)$ are included. For a better convergence the lowest β value was excluded from the dataset $\beta \in \{6.000, 6.284, 6.451, 6.594\}$, due to the non-negligible discretization errors. The gray dotted line marks the chosen scale $\nu_f = 1\mathrm{GeV}$. As one can see the difference between order n and $n+1$ gets significantly smaller for increasing orders. Therefore, the same behavior is expected for larger orders.
Evaluating the NNNLO fit at $\nu_f = 1\mathrm{GeV}$ for m_{II} results in

$$\Lambda_{\mathrm{B,fit}}^{\mathrm{RS}}(\nu_f = 1\ \mathrm{GeV}) = 1160(30)\mathrm{MeV}, \quad \chi^2/\mathrm{dof} = 0.097. \tag{93}$$

Note that the given error values are only determined via the NNNLO-fit with the given statistical uncertainties from the lattice mass results.

To get a better error estimation one has to sum up all possible sources of uncertainty:

1. $\sigma_{fit} = 30\text{MeV}$ is the error estimation of the NNNLO fit.

2. $\sigma_{\text{pert},1} = 50\text{MeV}$ is the expected error by ignoring terms of $\mathcal{O}(\alpha_s^4)$. The estimation of lower orders shows that the difference between two orders decreases approximately by a factor of three for every increment in the perturbation series, which leads to the given error.

3. $\sigma_{\text{pert},2} = 70\text{MeV}$ is due to the uncertainty in $N_{V_s} - N_{V_o}$ [13].

4. $\sigma_{\Lambda_{\overline{\text{MS}}}} = 40\text{MeV}$ is due to the error in $\Lambda_{\overline{\text{MS}}} r_0$[13].

Adding up these sources of uncertainty linearly leads to the final result for the mass of the magnetic gluelump (T_1^{+-}) in the RS scheme

$$\Lambda_B^{\text{RS}}(\nu_f = 1\text{GeV}) = 1160(190)\text{MeV}. \tag{94}$$

The calculation of the lowest-lying gluelump mass in [13] with the data computed in [3] led to $\Lambda_B^{\text{RS}}(\nu_f = 1\text{ GeV}) = 910(220)\text{MeV}$. Both results agree within error bands but suffer from a very high uncertainty, which is caused by the above-mentioned error sources. Even with more precise measurements on finer lattice spacings, the errors were just reduced insignificantly, since only a small fraction of the errors is caused by the lattice results themself.
To get a higher precision one has to expand equation (91) to higher orders and compute the parameters given in tabular 12 with more accuracy.

Parameter	Value	Definition
C_A	3	$f^{ACD}f^{BCD} = C_A\delta^{AB} = N_C\delta^{AB}$
v_1	$3.1759115\ldots$	Expansion coefficients of the static self-energy.
v_2	$0.21003(5) \times 10^3$	
v_3	$20.4(3) \times 10^3$	
b_1	$73.93539066\ldots$	Expansion coefficients for expressing α_L in units of α_s.
b_2	$b_1^2 + 1388.1645$	
β_0	$11C_A/3$	Expansion coefficients of the β-function for $n_f = 0$ [39].
β_1	$34C_A^2/3$	
$\tilde{V}_{s,1}$	-2.44378	Expansion coefficients of the singlet and octet potential divided by ν.
$\tilde{V}_{s,2}$	-11.7893	
$\tilde{V}_{o,1}$	0.305472	
$\tilde{V}_{o,2}$	1.27419	

Table 12: Definition of the coefficients used in equation (92). Every value without citation is taken from [13].

6.2.3 Comparison with other results

In table 13 the given summary taken from section 5.3 in reference [13] is shown. The calculated masses of the lightest gluelump range from 0.9GeV to 1.87GeV, which is in accordance with the results determined in the sections 6.2.1 and 6.2.2. Nevertheless, the given masses are all scheme dependent, which might be a main reason for the differences between different results. Additionally, some results are missing an error estimation, which makes a proper comparison even more difficult.

m in GeV	Method
≈ 1.87	String model
0.90(10)	Lattice simulations, using the cooling method
1.25(16)	Sum rule analysis of the magnetic correlator
≈ 1.37	MIT bag model
≈ 1.40	Constituent quark model

Table 13: Comparison with other calculation results of the lightest gluelump. The mass values, as well as the used method, were taken from [13]. The symbol $\approx$ denotes, that no errors were given.

7 Conclusion

7.1 Summary

The aim of this work was to compute precise gluelump masses in SU(3) lattice gauge and to compare them with hybrid static potentials. To guarantee an optimal overlap with the ground state for all 20 different $\Lambda^{\mathcal{PC}}$ gluelumps, APE-smearing was adapted such that the number of smearing steps was optimal for heavier gluelumps. Next, the multilevel parameters were adjusted for the T_1^{+-} gluelump, to enhance the results of the continuum extrapolation. For this purpose, the number of sublattice measurements was optimized for several different sublattice structures. On the one hand, uniform structures with varying time-slice thicknesses and number of levels were optimized. On the other hand, more complex constructs like the combination of several sublattices were considered. Even though for the final computations the simplest structure B $(= [1, 1, 1, 1, \dots])$ was chosen, the gained insights might be important for future computations.

Two different mass extraction procedures were applied to the correlation functions, which were computed on gauge field configurations with four different lattice spacings. While procedure *I* provides a qualitative insight into the ground state overlap, procedure *II* reduces the errors, but in some cases (e.g. A_2^{--}) the computed masses might be larger than the actual ground state mass. Besides that, the application of HYP-smearing, significantly improved mass difference results. Unfortunately, HYP-smeared gluelump masses turned out, to be not comparable with hybrid potentials, without any further adjustments.

A continuum extrapolation of mass differences with the assumption, that the discretization errors are of $\mathcal{O}(a^2)$ was successful. With the full gluelump spectrum, a unique spin identification was partly possible. A clear degeneracy for T_2 and E was found in two different $\mathcal{PC}$-sectors. Additionally, the computed continuum mass splittings were compared with the results of [3].

Since previously, only mass splittings were extrapolated to the continuum, two different approaches for the mass determination of the lightest gluelump T_1^{+-} were discussed. The conversion into the RS-scheme showed that more precise gluelump lattice masses do not significantly enhance the results, which is restricted by the power series expansion in α_s and the precision of coefficients.

In summary, the combination of optimized APE-smearing, adapted multilevel parameters, the application of HYP-smearing, and the mass extraction via two different procedures on four small lattice spacings, provided ground state results that are more trustworthy than former computations in literature (e.g. [3]).

7.2 Outlook

There are a few ways, how to improve the previously derived results. Even though choosing only one number of APE-smearing steps for all gluelumps reduces the total computation time significantly, a set of several different N_s would enhance the individual ground state results. Besides that, one can think of a large field of different multilevel sublattice structures, that might be more efficient than structure B. Additionally, structure optimizations on different lattice spacings would provide a deeper understanding of the multilevel algorithm in general and how optimal structures may be built. Besides that, one can think of a sublattice structure, where the spatial linear combinations $G(\tau)$ do not lie on the boundaries. This way the multilevel algorithm would not be restricted to the optimization of the temporal transporters, but could in general improve the whole gluelump correlator.
A unique spin identification requires a more comprehensive set of different operators that transform like Λ. With a clear spin identification a full analysis of the gluelump spectrum, like a possible $\mathcal{PC}$ dependence is possible.
Finally, the conversion into the RS-scheme has shown, that the results are mainly restricted by the power series expansion and its coefficients. Therefore, expanding equation (92) for higher orders and an improvement of the used coefficients would enhance the results. Since the errors of hybrid meson masses in [12] are dominated by the error of the gluelump mass in the RS-scheme, an improvement is important.
In summary, gluelumps provide an interesting field for further studies.

Appendices

A Additional results

In this section the gluelump mass results on each individual lattice spacing (cf. section 5.4.2) are collected.

$\Lambda^{\mathcal{PC}}$	m_{I}	χ^2/dof	m_{II}	χ^2/dof	$m_{\mathrm{I,HYP}}$	χ^2/dof	$m_{\mathrm{II,\,HYP}}$	χ^2/dof
T_1^{++}	2.184(20)	0.46	2.204(11)	0.85	1.636(18)	1.26	1.60(4)	0.38
T_1^{+-}	1.3316(20)	0.08	1.3319(17)	0.35	0.7699(18)	0.04	0.7705(15)	0.09
T_1^{-+}	1.932(12)	1.35	1.936(7)	1.38	1.372(11)	0.64	1.378(6)	0.91
T_1^{--}	1.485(5)	1.19	1.474(8)	0.84	0.936(4)	1.27	0.942(4)	1.91
T_2^{++}	2.049(18)	0.39	2.071(9)	0.13	1.491(17)	0.25	1.513(9)	0.09
T_2^{+-}	1.737(7)	0.84	1.735(9)	0.24	1.181(7)	0.55	1.181(8)	0.23
T_2^{-+}	2.009(19)	0.90	2.031(8)	0.99	1.441(19)	0.91	1.470(8)	0.95
T_2^{--}	1.569(5)	0.37	1.5763(21)	0.99	1.010(4)	1.10	1.0193(20)	0.65
A_1^{++}	1.750(13)	0.72	1.753(7)	0.34	1.191(12)	0.81	1.194(7)	0.16
A_1^{+-}	2.25(6)	0.92	2.276(27)	0.78	1.69(5)	0.57	1.720(25)	0.44
A_1^{-+}	2.27(6)	0.90	2.327(26)	1.02	1.73(5)	0.35	1.777(23)	0.50
A_1^{--}	1.963(15)	1.42	1.966(10)	0.23	1.402(15)	0.90	1.407(9)	0.43
A_2^{++}	2.31(4)	0.66	2.350(7)	0.57	1.76(4)	0.55	1.793(6)	0.60
A_2^{+-}	1.854(16)	1.55	1.887(8)	0.78	1.301(15)	1.27	1.306(20)	1.05
A_2^{-+}	2.056(22)	0.53	2.069(13)	0.19	1.500(21)	0.79	1.512(12)	0.05
A_2^{--}	2.05(9)	0.90	2.18(4)	3.65	1.70(5)	1.17	1.762(25)	3.54
E^{++}	1.878(20)	2.65	1.917(9)	2.13	1.330(18)	2.03	1.359(8)	0.77
E^{+-}	1.730(9)	0.41	1.726(12)	0.33	1.171(8)	0.80	1.165(11)	0.84
E^{-+}	1.985(22)	1.37	2.014(10)	2.32	1.434(20)	1.27	1.460(10)	1.51
E^{--}	1.566(6)	0.91	1.563(6)	0.24	1.007(6)	0.96	1.006(6)	0.80

Table 14: Lattice results with errors and χ^2/dof for $\beta = 6.0$. The subscripts I and II denote the used procedure for the mass extraction, while HYP indicates, that HYP-smearing was applied. All results are given in units of the lattice spacing a.

$\Lambda^{\mathcal{PC}}$	m_{I}	χ^2/dof	m_{II}	χ^2/dof	$m_{\mathrm{I,HYP}}$	χ^2/dof	$m_{\mathrm{II,\,HYP}}$	χ^2/dof
T_1^{++}	1.652(12)	0.88	1.653(10)	0.88	1.150(9)	0.95	1.155(6)	1.02
T_1^{+-}	1.0805(18)	0.85	1.0816(14)	0.96	0.5774(13)	1.29	0.5784(13)	1.90
T_1^{-+}	1.465(10)	0.51	1.475(6)	0.63	0.971(7)	0.62	0.966(8)	0.91
T_1^{--}	1.1955(30)	0.62	1.188(8)	0.57	0.6984(19)	0.55	0.692(5)	0.30
T_2^{++}	1.584(11)	0.74	1.598(4)	0.77	1.071(9)	0.51	1.080(6)	0.57
T_2^{+-}	1.362(6)	0.65	1.3671(30)	0.70	0.863(4)	0.47	0.860(4)	0.64
T_2^{-+}	1.540(13)	0.99	1.552(8)	0.83	1.039(9)	1.18	1.055(5)	1.87
T_2^{--}	1.242(4)	0.63	1.243(4)	0.33	0.7350(26)	3.34	0.735(4)	1.13
A_1^{++}	1.361(10)	0.69	1.374(4)	0.69	0.872(6)	0.68	0.873(5)	0.47
A_1^{+-}	1.720(22)	0.73	1.740(9)	0.31	1.226(14)	0.95	1.230(15)	0.32
A_1^{-+}	1.776(20)	0.66	1.789(8)	0.96	1.272(14)	0.54	1.275(14)	0.15
A_1^{--}	1.499(10)	0.71	1.501(9)	1.22	0.974(9)	1.11	0.988(6)	1.18
A_2^{++}	1.692(27)	0.75	1.732(8)	1.24	1.195(18)	0.56	1.202(14)	0.62
A_2^{+-}	1.414(16)	0.94	1.453(8)	2.35	0.916(10)	2.96	0.933(10)	3.45
A_2^{-+}	1.539(20)	0.61	1.555(12)	0.79	1.065(9)	0.31	1.069(8)	0.46
A_2^{--}	1.57(5)	0.66	1.60(4)	0.02	1.262(14)	1.59	1.267(14)	1.09
E^{++}	1.466(9)	0.71	1.465(8)	0.07	0.968(7)	0.98	0.972(5)	0.93
E^{+-}	1.351(6)	1.24	1.348(8)	0.76	0.852(4)	0.93	0.853(5)	0.41
E^{-+}	1.527(13)	1.90	1.531(9)	0.58	1.037(7)	0.42	1.038(6)	1.25
E^{--}	1.236(5)	1.49	1.227(8)	0.57	0.735(4)	0.59	0.727(5)	0.44

Table 15: Lattice results with errors and χ^2/dof for $\beta = 6.284$. The subscripts I and II denote the used procedure for the mass extraction, while HYP indicates, that HYP-smearing was applied. All results are given in units of the lattice spacing a.

$\Lambda^{\mathcal{PC}}$	m_{I}	χ^2/dof	m_{II}	χ^2/dof	$m_{\mathrm{I,HYP}}$	χ^2/dof	$m_{\mathrm{II,\ HYP}}$	χ^2/dof
T_1^{++}	1.441(7)	1.01	1.451(4)	0.49	0.971(6)	0.97	0.980(4)	0.39
T_1^{+-}	0.9714(12)	0.69	0.9711(9)	0.64	0.4997(11)	0.73	0.4996(8)	0.92
T_1^{-+}	1.281(7)	0.93	1.292(4)	0.95	0.810(6)	1.04	0.821(4)	1.04
T_1^{--}	1.0643(17)	0.33	1.0627(26)	0.29	0.5941(16)	0.56	0.5913(25)	0.20
T_2^{++}	1.365(8)	0.30	1.3823(30)	0.90	0.895(8)	0.37	0.9116(29)	0.96
T_2^{+-}	1.200(4)	0.77	1.198(4)	0.18	0.728(4)	0.34	0.726(4)	0.43
T_2^{-+}	1.332(9)	2.42	1.3597(26)	2.52	0.862(8)	2.25	0.8889(25)	3.05
T_2^{--}	1.0922(29)	0.72	1.0958(20)	0.73	0.6206(28)	1.05	0.6251(19)	1.35
A_1^{++}	1.195(7)	0.70	1.201(5)	0.21	0.725(7)	0.32	0.730(5)	0.27
A_1^{+-}	1.465(15)	0.48	1.486(7)	0.49	0.999(13)	0.28	1.017(7)	0.45
A_1^{-+}	1.538(12)	1.94	1.551(7)	0.14	1.070(11)	1.44	1.082(7)	0.09
A_1^{--}	1.307(6)	0.44	1.314(4)	0.80	0.837(6)	1.66	0.844(4)	0.80
A_2^{++}	1.490(12)	0.86	1.500(7)	0.20	1.019(11)	0.68	1.029(7)	0.25
A_2^{+-}	1.269(9)	0.66	1.286(6)	1.63	0.788(9)	0.98	0.796(9)	1.66
A_2^{-+}	1.347(10)	0.45	1.351(8)	0.38	0.874(10)	0.51	0.879(8)	0.47
A_2^{--}	1.25(4)	0.58	1.27(4)	0.07	1.031(14)	1.37	1.059(7)	1.79
E^{++}	1.271(7)	1.03	1.2820(28)	2.53	0.800(7)	0.88	0.8106(27)	2.64
E^{+-}	1.186(4)	0.91	1.182(5)	0.31	0.7153(29)	0.81	0.7185(27)	1.21
E^{-+}	1.298(12)	1.56	1.3396(29)	6.99	0.829(11)	2.40	0.8686(29)	6.54
E^{--}	1.096(4)	1.60	1.091(4)	0.16	0.6258(29)	1.29	0.621(4)	0.26

Table 16: Lattice results with errors and χ^2/dof for $\beta = 6.451$. The subscripts I and II denote the used procedure for the mass extraction, while HYP indicates, that HYP-smearing was applied. All results are given in units of the lattice spacing a.

$\Lambda^{\mathcal{PC}}$	m_{I}	χ^2/dof	m_{II}	χ^2/dof	$m_{\mathrm{I,HYP}}$	χ^2/dof	$m_{\mathrm{II,\ HYP}}$	χ^2/dof
T_1^{++}	1.277(7)	0.68	1.286(4)	1.05	0.826(6)	0.80	0.8355(30)	1.22
T_1^{+-}	0.8976(10)	0.92	0.8942(21)	0.23	0.4471(9)	1.57	0.4488(7)	1.20
T_1^{-+}	1.160(6)	1.61	1.165(6)	0.83	0.708(6)	2.15	0.7229(21)	1.91
T_1^{--}	0.9713(13)	0.79	0.9670(26)	0.25	0.5219(12)	0.90	0.5200(13)	0.35
T_2^{++}	1.248(5)	0.27	1.2480(29)	0.99	0.796(5)	0.40	0.7981(28)	0.96
T_2^{+-}	1.0908(22)	0.76	1.0872(27)	0.33	0.6411(20)	0.81	0.6374(26)	1.01
T_2^{-+}	1.221(5)	0.91	1.2225(26)	0.90	0.770(4)	1.01	0.768(5)	0.97
T_2^{--}	1.0012(21)	1.01	0.9982(22)	0.21	0.5521(18)	0.78	0.5513(15)	0.81
A_1^{++}	1.101(4)	1.74	1.0986(24)	0.33	0.650(4)	0.25	0.6484(24)	0.32
A_1^{+-}	1.338(9)	1.09	1.345(8)	0.86	0.891(8)	0.33	0.902(4)	1.11
A_1^{-+}	1.369(9)	0.66	1.370(7)	0.21	0.919(9)	0.89	0.930(4)	0.87
A_1^{--}	1.178(5)	0.74	1.1807(29)	1.09	0.729(4)	0.61	0.7306(29)	0.83
A_2^{++}	1.333(9)	0.85	1.328(7)	0.31	0.883(8)	1.10	0.878(7)	0.55
A_2^{+-}	1.146(8)	1.14	1.155(5)	0.95	0.692(8)	0.88	0.707(5)	0.88
A_2^{-+}	1.208(8)	0.43	1.206(7)	0.61	0.761(7)	0.63	0.769(4)	1.36
A_2^{--}	1.073(27)	0.76	1.07(4)	0.44	0.906(10)	0.57	0.910(7)	0.62
E^{++}	1.161(4)	0.47	1.1593(28)	0.16	0.710(4)	0.55	0.7113(17)	0.54
E^{+-}	1.0774(22)	0.37	1.073(4)	0.02	0.6277(20)	0.42	0.6308(15)	0.96
E^{-+}	1.210(4)	0.80	1.2091(29)	0.46	0.759(4)	0.56	0.7583(29)	0.12
E^{--}	1.0105(17)	0.30	1.0094(15)	0.86	0.5611(16)	0.39	0.5598(14)	1.10

Table 17: Lattice results with errors and χ^2/dof for $\beta = 6.594$. The subscripts I and II denote the used procedure for the mass extraction, while HYP indicates, that HYP-smearing was applied. All results are given in units of the lattice spacing a.

Danksagung

An dieser Stelle möchte ich all denjenigen danken, die mich während der Erarbeitung und anschließenden Anfertigung meiner Masterarbeit so hilfreich unterstützt haben.

Dank der tollen Betreuung von Prof. Dr. Marc Wagner konnte ich einen noch besseren Einblick in das wissenschaftliches Denken und Arbeiten erhalten. Die zahlreichen persönlichen Gespräche waren sehr aufschlussreich für mich. Selbst in stressigen Momenten nahm sich Prof. Dr. Marc Wagner stets die Zeit für ein spontanes Skype-Meeting, das mich und meine Arbeit weiterbrachte.

Ebenfalls möchte ich sowohl Christian Reisinger für die Bereitstellung des Multilevel-Codes als auch Michael Eichberg für die große Hilfe bei der Installation und die Klärung erster Fragen danken. Außerdem danke ich Carolin Schlosser für die Bereitstellung der SU(3)-Konfigurationen und weitere hilfreiche Tipps für die Installation.

Zuletzt gilt mein Dank Jonas Winter, Marius Kunold und Marcel Hübner für ihre konstruktiven Korrekturvorschläge.

References

[1] Carolin Schlosser and Marc Wagner. "Hybrid static potentials in SU(3) lattice gauge theory at small quark-antiquark separations". In: (2021). arXiv: 2111.00741 [hep-lat].

[2] I.H. Jorysz and C. Michael. "The Field Configurations Of A Static Adjoint Souce in SU(") Lattice Gauge Theory". In: *Nucl. Phys. B* 302 (1987), pp. 448–470.

[3] M. Foster and C. Michael. "Hadrons with a heavy color-adjoint particle". In: *Physical Review D* 59.9 (1999). ISSN: 1089-4918. DOI: 10.1103/physrevd.59.094509. URL: http://dx.doi.org/10.1103/PhysRevD.59.094509.

[4] Philipp Wolf. "Gluelump Massenberechnung in der SU(2) Yang-Mills-Theorie". In: *BA thesis* (2020).

[5] Jannis Herr. "Gluelump Massenberechnung in der SU(3) Yang-Mills Gittereichtheorie". In: *BA thesis* (2020).

[6] Kristen Marsh and Randy Lewis. "Lattice QCD study of generalized gluelumps". In: *Physical Review D* 89.1 (2014). ISSN: 1550-2368. DOI: 10.1103/physrevd.89.014502. URL: http://dx.doi.org/10.1103/PhysRevD.89.014502.

[7] Gabriel Karl and Jack Paton. "Gluelump spectrum in the bag model". In: *Physical Review D* 60.3 (1999). DOI: 10.1103/physrevd.60.034015. URL: https://doi.org/10.1103%2Fphysrevd.60.034015.

[8] Yu.A. Simonov. "Gluelump spectrum in the QCD string model". In: *Nuclear Physics B* 592.1-2 (2001), pp. 350–368. DOI: 10.1016/s0550-3213(00)00592-7. URL: https://doi.org/10.1016%2Fs0550-3213%2800%2900592-7.

[9] Peng Guo et al. "Gluelump spectrum from Coulomb gauge QCD". In: *Physical Review D* 77.5 (2008). DOI: 10.1103/physrevd.77.056005. URL: https://doi.org/10.1103%2Fphysrevd.77.056005.

[10] Christian Szasz and Marc Wagner. "Adjoint string breaking in the pseudoparticle approach". In: *Physical Review D* 78.3 (2008). ISSN: 1550-2368. DOI: 10.1103/physrevd.78.036006. URL: http://dx.doi.org/10.1103/PhysRevD.78.036006.

[11] Yu.A. Simonov. "Gluelump spectrum in the QCD string model". In: *Nuclear Physics B* 592.1-2 (2001), pp. 350–368. ISSN: 0550-3213. DOI: 10.1016/s0550-3213(00)00592-7. URL: http://dx.doi.org/10.1016/S0550-3213(00)00592-7.

[12] Matthias Berwein et al. "Quarkonium hybrids with nonrelativistic effective field theories". In: *Physical Review D* 92.11 (2015). ISSN: 1550-2368. DOI: 10.1103/physrevd.92.114019. URL: http://dx.doi.org/10.1103/PhysRevD.92.114019.

[13] Gunnar S. Bali and Antonio Pineda. "QCD phenomenology of static sources and gluonic excitations at short distances". In: *Physical Review D* 69.9 (2004). ISSN: 1550-2368. DOI: 10.1103/physrevd.69.094001. URL: http://dx.doi.org/10.1103/PhysRevD.69.094001.

[14] Martin Lüscher and Peter Weisz. "Locality and exponential error reduction in numerical lattice gauge theory". In: *Journal of High Energy Physics* 2001.09 (2001), pp. 010–010. ISSN: 1029-8479. DOI: 10.1088/1126-6708/2001/09/010. URL: http://dx.doi.org/10.1088/1126-6708/2001/09/010.

[15] C. Gattringer and C.B. Lang. *Quantum Chromodynamics on the Lattice*. Springer, 2010.

[16] Christian Reisinger. "Hybrid static potentials in SU(3) gauge theory on the lattice". MA thesis. Johann Wolfgang Goethe-Universität, Fachbereich Physik Institut für Theoretische Physik, 2017.

[17] Chris Michael. "Adiabatic surfaces from the lattice: excited gluonic potentials". In: *High Energy Physics - Phenomenology (hep-ph)* LTH 435 (1998).

[18] Dirk H. Rischke. *Theoretische Physik VI: Quantenmechanik II*. Institut für theoretische Physik, Goethe Universität Frankfurt am Main, 2016.

[19] Grigorios I Poulis and Howard D Trottier. ""Gluelump" spectrum and adjoint source potential in lattice QCD3". In: *Physics Letters B* 400.3-4 (1997), pp. 358–363. ISSN: 0370-2693. DOI: 10.1016/s0370-2693(97)88182-8. URL: http://dx.doi.org/10.1016/S0370-2693(97)88182-8.

[20] Chris Michael. "Adjoint sources in lattice gauge theory". In: *Nucl. Phys. B* 259.1985 (1985), pp. 58–76.

[21] B. Berg and A. Billoire. "Glueball Spectroscopy in 4d SU(3) Lattice Gauge Theory". In: *Nuclear Physics B* 221 (1983), pp. 109–140.

[22] R.C. Johnson. "Angular Momentum on a Lattice". In: *Physics Letters* 114B (1982).

[23] K. Demmouche. *Symmetries On The Lattice*. 2006. URL: https://www.uni-muenster.de/Physik.TP/archive/fileadmin/lehre/QFT/cubic-group.pdf.

[24] Robert G. Petry et al. "Exploring the meson spectrum with twisted mass lattice QCD". In: *Physical Review D* 78.7 (2008). ISSN: 1550-2368. DOI: 10.1103/physrevd.78.074502. URL: http://dx.doi.org/10.1103/PhysRevD.78.074502.

[25] Chris Michael. "The Glueball spectrum from lattice gauge theory". In: *ACTA PHYSICA POLONICA* B21.2 (1990).

[26] Kristen Allana Marsh. "Spectrum of Gluelumps Containing Various QCD Spectrum of Gluelumps Containing Various QCD Colour-Multiplet Particles". PhD thesis. York University Toronto, Ontario, 2013.

[27] M. Albanese et al. [APE Collaboration]. "Glueball Masses and String Tension in Lattice QCD". In: *Phys. Lett. B* 192, 163 (1987).

[28] Stephan Dürr. "Gauge action improvement and smearing". In: *Computer Physics Communications* 172.3 (2005), pp. 163–186. ISSN: 0010-4655. DOI: 10.1016/j.cpc.2005.06.011. URL: http://dx.doi.org/10.1016/j.cpc.2005.06.011.

[29] G. Peter Lepage. "Simulating heavy quarks". In: *Nucl. Phys. B Proc. Suppl.* 26 (1992), pp. 45–56. DOI: 10.1016/0920-5632(92)90228-K.

[30] Anna Hasenfratz and Francesco Knechtli. "Flavor symmetry and the static potential with hypercubic blocking". In: *Physical Review D* 64.3 (2001). ISSN: 1089-4918. DOI: 10.1103/physrevd.64.034504. URL: http://dx.doi.org/10.1103/PhysRevD.64.034504.

[31] Nora Brambilla et al. "Lattice gauge theory computation of the static force". In: (2021). arXiv: 2106.01794 [hep-lat].

[32] Owe Philipsen et al. "CL2QCD - Lattice QCD based on OpenCL". In: (2014). DOI: 10.48550/ARXIV.1411.5219. URL: https://arxiv.org/abs/1411.5219.

[33] Silvia Necco and Rainer Sommer. "The Nf=0 heavy quark potential from short to intermediate distances". In: *Nuclear Physics B* 622.1-2 (2002), pp. 328–346. DOI: 10.1016/s0550-3213(01)00582-x. URL: https://doi.org/10.1016%2Fs0550-3213%2801%2900582-x.

[34] Peter Young. *Everything you wanted to know about Data Analysis and Fitting but were afraid to ask*. 2012. DOI: 10.48550/ARXIV.1210.3781. URL: https://arxiv.org/abs/1210.3781.

[35] Colin J. Morningstar and Mike Peardon. "Glueball spectrum from an anisotropic lattice study". In: *Physical Review D* 60.3 (1999). DOI: 10.1103/physrevd.60.034509. URL: https://doi.org/10.1103%2Fphysrevd.60.034509.

[36] Silvia Necco. "The static quark potential and scaling behavior of SU(3) lattice Yang-Mills theory". PhD thesis. Humbolt-Universität Berlin, 2003.

[37] B. Blossier et al. "Efficient use of the Generalized Eigenvalue Problem". In: (2008). DOI: 10.48550/ARXIV.0808.1017. URL: https://arxiv.org/abs/0808.1017.

[38] G. Peter Lepage and Paul B. Mackenzie. "Viability of lattice perturbation theory". In: *Physical Review D* 48.5 (1993), pp. 2250–2264. ISSN: 0556-2821. DOI: 10.1103/physrevd.48.2250. URL: http://dx.doi.org/10.1103/PhysRevD.48.2250.

[39] M. Czakon. "The four-loop QCD β-function and anomalous dimensions". In: *Nuclear Physics B* 710.1-2 (2005), pp. 485–498. ISSN: 0550-3213. DOI: 10.1016/j.nuclphysb.2005.01.012. URL: http://dx.doi.org/10.1016/j.nuclphysb.2005.01.012.